Icarus **158**, 224–248 (2002)
doi:10.1006/icar.2002.6852

A Study of Saturn's Ring Phase Curves from HST Observations

F. Poulet and J. N. Cuzzi

NASA Ames Research Center, MS 245/3, Moffett Field, California 94035
E-mail: poulet@vimstlm.obspm.fr

R. G. French

Astronomy Department, Wellesley College, Wellesley, Massachusetts 02481

and

L. Dones

Southwest Research Institute, 1050 Walnut Street, Boulder, Colorado 80302

Received May 18, 2001; revised September 12, 2001

Solar phase curves between 0.3° and 6.0° and color ratios at wavelengths $\lambda = 0.336$ μm and $\lambda = 0.555$ μm for Saturn's rings are presented using recent Hubble Space Telescope observations. We test the hypothesis that the phase reddening of the rings is less due to collective properties of the ring particles than to the individual properties of the ring particles. We use a modified Drossart model, the Hapke model, and the Shkuratov model to model reddening by either intraparticle shadow-hiding on fractal and normal surfaces, multiple scattering, or some combination. The modified Drossart model (including only shadowing) failed to reproduce the data. The Hapke model gives fair fits, except for the color ratios. A detailed study of the opposition effect suggests that coherent backscattering is the principal cause of the opposition surge at very small phase angles. The shape of the phase curve and color ratios of each main ring regions are accurately represented by the Shkuratov model, which includes both a shadow-hiding effect and coherent backscatter enhancement. Our analysis demonstrates that in terms of particle roughness, the C ring particles are comparable to the Moon, but the Cassini division and especially the A and B ring particles are significantly rougher, suggesting lumpy particles such as often seen in models. Another conspicuous difference between ring regions is in the effective size d of regolith grains ($d \sim \lambda$ for the C ring particles, $d \sim 1-10$ μm for the other rings).

Key Words: **planetary rings; Saturn—phase curve; opposition effect—shadow-hiding, coherent backscattering.**

1. INTRODUCTION

In spite of the flybys by the Voyager spacecraft and numerous ground-based observations, some fundamental questions concerning Saturn's rings remain unanswered. While there are numerous models of the ring particle size distribution in the cm–10 m radius range (Marouf *et al.* 1983, Zebker *et al.* 1985, French and Nicholson 2000), it is not clear whether these particles are "dynamic ephemeral bodies" in a statistical equilibrium, accreting and fragmenting on a time scale of weeks (Weidenshilling *et al.* 1984) or hard ice balls (Shu *et al.* 1985). Much can be learned about the nature of ring particles and their regolith by modeling the change of brightness with viewing geometry, and in particular with the phase angle. While these variations can be understood in terms of the properties of a multiply-scattering regolith for other atmosphereless bodies in the Solar System, direct comparison of brightness profiles across varying geometries is complicated in the case of Saturn's rings by the facts that the ring brightness varies with illumination and viewing geometries and optical depth.

A recent campaign of observation of Saturn's rings with the Hubble Space Telescope (HST) Wide Field Planetary Camera 2 done by Cuzzi *et al.* (2001) (henceforth CFD01) was particularly useful to disentangle whether individual or collective properties of the ring particles could create the variation of brightness observed with illumination and viewing geometry. With a spread of phase angles between 0.3° and 6° at different ring opening angles between 4° and 18°, the data showed that the geometrical dependence of color variations is confined almost entirely to phase angle and almost lacking with the ring opening angle. This implies that the collective properties of the ring particles are less important than the individual properties of the ring particles in the considered geometry.

In view of these new HST observations, this paper presents an analysis of the phase curves of four main rings (A, B, C rings and Cassini division) in order to derive the properties of the surfaces of the ring particles. One of the observed behaviors of the phase curves is the opposition effect (hereafter OE), a sharp increase in the reflectance as the phase angle approaches zero. It has long been known that Saturn's A and B rings exhibit pronounced

0019-1035/02 $35.00

photometric opposition effects (Franklin and Cook 1965), but their origin is still not clear. Mutual shadowing among the macroscopic ring bodies was first invoked to reproduce the angular width of this OE, but this mechanism requires that Saturn's A and B rings are many-particles-thick and that the volume density D of the rings is very small ($D = 0.020 \pm 0.04$ according to Lumme *et al.* 1983). Such results contradict recent dynamical models for realistic inelastic ring particles, which imply a relatively high volume density (Salo 1987, 1992, Richardson 1994). Moreover, in the light of new HST observations, the explanation of the OE should be more due to effects on the individual ring particle surfaces than due to interparticle scattering effects. An alternate explanation for the OE was proposed by Mishchenko and Dlugach (1992) who showed that the OE could be consistent with coherent backscattering if the effective radius of regolith grains was about 0.1–1 μm. However, this effective grain size is much smaller than that derived from spectroscopic observations (Pollack *et al.* 1973, Clark and McCord 1980, Doyle *et al.* 1989, Alix 1998). The OE could be also explained in terms of the shadow-hiding effect, in which regolith grains occult their own shadows (Hapke 1986), but this has not been investigated to date.

The first attempt to model the phase function of the main rings was by Dones *et al.* (1993), using Voyager images of the A ring. However, this early work merely assumed a power-law particle phase function, which was empirical and not directly related to the physical properties of the scattering surface. Moreover, the important effects of multiple scattering between the particles at large phase angles did not seem to be well fit by the models.

In this paper, using only low phase angle data, which are apparently uncontaminated by multiple interparticle scattering, we try to model the ring particle phase curves and to constrain the origin of the opposition surge. Information about the roles of multiple regolith grain scattering and shadow-hiding can be derived from studying how photometric properties of regolith materials vary with wavelength. The very well-sampled HST data studied here allows us to select phase curves at 0.336 and 0.555 μm, a range of wavelength in which the spectrum of rings is strongly red. Estimates will be made of the regolith characteristics such as grain size, surface roughness and porosity, and/or other parameters depending on the model used.

There are three major sections to this paper. First, we present the analyzed data and then, we review the main conclusions of CFD01 which lead us to present some motivations for modeling the exotic phase curves of Saturn's rings. In Section 3, the models of phase curves used here are presented and discussed. Section 4 consists of derivation of photometric parameters, some discussion, and interpretation of the results in terms of the properties of particle surfaces.

2. DATA AND SOME REMARKS

Our starting point is a description of the data used to study the phase curves of rings. The images analyzed here were taken during an intensive campaign of Saturn's rings with HST from September 1996 to October 1998. The image processing is described in CFD01, so that we present the conditions of illumination of rings of the selected images only. In addition, we review some conclusions of CFD01. Then, the various theoretical models of photometric observations are presented.

2.1. Data Set

The geometry for the illumination of the rings by the Sun is defined by the three following angles:

- The subsolar latitude relative to the ring plane, B' (with $\mu' \equiv \sin B'$).
- The sub-Earth latitude relative to the ring plane, B (with $\mu \equiv \sin B$).
- The phase angle α, defined as the Sun–rings–Earth angle.

At each of four B and B' angles between 4° and 18°, and for phase angles ranging between 0.3° and 6.0°, Wide Field Planetary Camera 2 images of the rings in five standard UBVRI filters were obtained (see CFD01). Images were selected from this data set to encompass the broadest possible distribution of phase angle at different wavelengths. Although CFD01 has shown that the ring color is almost independent of B and B' (see next section), we preferred to analyze images with values of B and B' lying in a limited range. At Earth and Sun elevation angles of about 10°, the data were sufficiently well sampled to get five phase angles, $\alpha = 0.3$, 0.5, 1, 2, and 6° in two filters (U and V filters). Table I lists the condition of illumination of selected images.

Before modeling the data, we review the main conclusions of CFD01 about the variation of the ring brightness with geometry.

2.2. A Short Review of CFD01 and Some Consequences

The analysis of the HST data by our companion paper CFD01 has clarified the effects of angles B, B', and α on the brightness of rings:

- CFD01 argues that multiple interparticle scattering contributes only a small amount of light in any of the Earth-based

TABLE I
Observation Log

Date	α (°)	B (°)	B' (°)	Filter
1997 Oct 10	0.30	−9.99	−10.28	F336W
1997 Oct 10	0.30	−9.99	−10.28	F555W
1997 Oct 6	0.50	−10.12	−10.22	F336W
1997 Oct 6	0.50	−10.12	−10.22	F555W
1997 Oct 1	0.98	−10.28	−10.15	F336W
1997 Oct 1	0.98	−10.28	−10.15	F555W
1997 Sep 22	2.00	−10.59	−10.01	F336W
1997 Sep 22	2.00	−10.59	−10.01	F555W
1998 Jan 1	6.02	−8.88	−11.47	F336W
1998 Jan 1	6.02	−8.88	−11.47	F555W

geometries. We review their arguments here very briefly. The "classical" interpretation of ring brightness variations with ring opening angle is that multiple scattering *between* ring particles increases in importance as the rings open up (e.g., Lumme and Irvine 1976, Esposito and Lumme 1977, Lumme *et al.* 1983). The HST observations of CFD01 shows that the brightness of most A and C rings, and even the inner B ring, is in perfectly good agreement with a classical single-scattering model. The outer two-thirds of the B ring, however, does increase in brightness to a greater extent as the rings open up than can be explained by a classical single-scattering model. The classical explanation for this is that multiple scattering *between* ring particles increases in these geometries, as the Sun illuminates deeper regions within the rings. However, CFD01 shows that the *color* of the rings remains essentially independent of opening angle, with at most a few percent increase at the very largest opening angles and phase angles. This is inconsistent with the significant (25%) multiple scattering contribution implied by classical models (e.g., Lumme *et al.* 1983; see CFD01 for details). Furthermore, doubling code calculations for backscattering particles with moderate albedos, such as best fit, the B ring particles (Doyle *et al.* 1989) show that the multiple scattering contribution is very small in Earth-based geometries (Cuzzi *et al.* 1984). Instead, CFD01 suggests that the anomalous B ring brightness increase with increasing opening angle is due to nonclassical layer structure—perhaps the particles are not well separated and/or the ring is not many particles thick (Dones *et al.* 1993). CFD01 suggests that phase reddening is due to another form of multiple scattering acting within the surfaces of individual particles, or at most nearest neighbors—illumination of shadowed facets by nearby lit ones, which are reddish in color relative to the sun.

- The ring phase reddening between 0.3° and 6.0° is stronger than other icy planetary objects. While all prior studies seemed to indicate that color dependence of phase function is at best very small, this is clearly not an appropriate assumption for the rings.

If scattering between different particles can be neglected, we have to explain the observations using scattering within the surface of the individual ring particles only. Our approach is to use the photometric models developed for the study of the phase curves of planetary surfaces without atmospheres. The surface of a ring particle is certainly very different from the surface of large satellites in terms of size and shape. Therefore, the question arises whether we can use the usual photometric models for our study. First, we believe that the presence of a grainy regolith on the ring particles (larger than one centimeter and so) similar to that which covers the planetary satellites is realistic and plausible. Snowballs have grainy regoliths. The shape and depth of water ice absorption bands in the rings have been modeled for decades in terms of grainy regoliths on the ring particles. Spokes in Saturn's rings are very well modeled by small particles, which are plausibly supplied from loose material covering the surfaces of macroscopic particles. Collisions and constant micrometeoroid bombardment of the ring particles make grainy regoliths. For these reasons, we think that we can make the assumption that ring particles are covered by a grainy regolith. Regarding the shape and the size, it is likely that the ring particles have macroscopically irregular, lumpy, grape-clustered surfaces, considering the structure or appearance of "ring particles" as seen in accretional simulations (Salo 1992, Richardson 1994). This could raise questions about the validity of disk-integrated brightness. However, by investigating the light reflected by aggregates of aggregates of spherical or irregular particles, Alix (1998) showed that the phase curves of aggregates are not exotic, but similar to the phase curve of an elementary macroscopic particle constituting the aggregates. More important, the photometric study of the A ring by Dones *et al.* (1993) revealed that the phase function of A ring particles was very similar to those of icy satellites for phase angles larger than 15°. Consequently, we see no reason why the size, the size distribution, or the shape could prevent us from representing ring particle surfaces with the usual models.

The increase of color index $C(0.555/0.336)$ with increasing α can be explained in terms of either an unusual amount of wavelength-dependent dilution of the shadow-hiding effect and/or an unusual amount of multiple scattering in the regolith. A model of shadowing effects was first proposed by Irvine (1966). It has been discussed by a number of researchers and increasingly accurate photometric functions were proposed (Lumme and Bowell 1981a, 1981b, Hapke 1981, 1984) in order to take into account various aspects of the morphology of the surface. Despite the good agreement between these models and observations of numerous atmosphereless bodies, there are still many unsolved questions about the interpretation of the model parameters in terms of the physical structure of the regolith. A new approach has been recently proposed which is to approximate the surface by a fractal (Drossart 1993, Shkuratov *et al.* 1999). The idea to represent a ring particle by a self-similar object seems natural. Constructed of aggregates of aggregates, ring particles may well have many re-entrant surfaces with deep shadows, facets illuminating other facets, and so on which are not well treated by existing models. The second effect able to explain the increase of $C(0.555/0.336)$ with α might be a higher-order scattering contribution within each facet or between regolith grains; the higher the albedo of a surface, the greater this contribution. Therefore, one can expect that a more colored surface has a more pronounced phase dependence of color. Saturn's rings are very good candidates to check this suggestion because the rings are very red in the range of wavelength considered. CFD01 notes that, in wavelength regions where the spectrum is flat, no phase reddening is seen.

The light backscattered from Saturn's rings at small phase angles (below 1°) is marked by the OE, a nonlinear increase in brightness as opposition is approached. Again, this effect could be the result of the shadow-hiding effect (Hapke 1986, Hillier 1997) and/or of a second effect called coherent backscattering

(Muinonen 1989, Hapke 1990, Mishchenko and Dlugach 1992, 1993, Mishchenko 1993, Shkuratov *et al.* 1996, 1999). In the shadow-hiding opposition effect (hereafter SHOE), the surge is caused by the fact that the regolith particles completely occult their own shadows at small α, but the shadows become more visible with increasing α. In the coherent backscattering opposition effect (hereafter CBOE), light rays which travel identical but reversed paths in a surface emerge in phase and interfere constructively leading to up to a factor of two increase in brightness at opposition. The CBOE is believed to be most important for high albedo regoliths because it depends on multiple scattering of photons through and between scatterers. However, CB is still not understood theoretically, and several recent experiments and observations do not agree with the theoretical results. Even low-albedo materials can exhibit a significant CBOE (Nelson *et al.* 1998, Shkuratov *et al.* 1999, Belskaya and Shevchenko 2000). More surprising, measurements of the backscattering light by snow managed by Piironen *et al.* (2000) show that the opposition spike is more pronounced for the dirtier snow. Such observations complicate a lot the interpretation of data and the understanding of CB because, according to the theory widely accepted, darkening the snow should lower the multiple scattering, and so lower the OE. The authors interpret their measurements as a result of the surface hoar and/or of the microstructures of individual dark coarse grains. The size of regolith particles can also affect this mechanism significantly, the opposition effect being more pronounced for smaller size particles with a weak maximum for the particle size close to the wavelength of the incident light (Shkuratov *et al.* 1997, 1999, Nelson *et al.* 2000). These experiments disagree with the theoretical computation of Mishchenko and Dlugach (1992). Finally, the CBOE is also found very sensitive to the particle shape and the filling factor (Liang and Mishchenko 1997). While the OE of Saturn's A and B rings may be explained by the CB mechanism (Mishchenko and Dlugach 1992, Mishchenko 1993), it is essential to reinterpret the opposition effect of Saturn's rings in the light of these recent results on the CB. Moreover, no data or analysis have previously been reported for the C ring and the Cassini division, where the albedo of particles are similar to dirty snow.

Some papers are devoted to a discussion on the relative contribution of both mechanism (Helfenstein *et al.* 1997, 1998, Hapke *et al.* 1998, Nelson *et al.* 1998, Belskaya and Shevchenko 2000). A test of coherent backscatter and shadow-hiding effect theories can be derived by studying the influence of the albedo and the wavelength of incident light on the opposition brightness effect. Both the amplitudes A and the half-width at half-maximum *HWHM* of the opposition peak depend on the albedos. As shown in Section 4, the values of these parameters are model-dependent. Shkuratov *et al.* (1996, 1999) identified an anomalous opposition color effect in measurements of color index of some lunar soils and a spectral analogue of the Martian soil: the color index decreases with decreasing phase angle and then rises at small phase angles (in general less than a few degrees). The authors interpret the rise as a signature of the coherent backscattering. Our data set covering two wavelengths should allow us to distinguish the coherent backscatter from the shadow-hiding effects.

3. RADIATIVE TRANSFER MODELS

The photometric modeling of phase curves and color index of rings is based on the relations derived by Hapke (1981, 1984, 1986), Drossart (1993), and Shkuratov *et al.* (1999), respectively. Our strategy is to determine whether the light backscattering from Saturn's ring particles can be best explained by the physical processes presented in Section 2.2, i.e., either by shadow-hiding (hereafter SH) on a "normal surface" with an opposition surge attributed to SH (Hapke model), by SH on a fractal surface with no particular treatment of the OE (Drossart model), or by SH with an opposition surge spike caused by CB on a fractal surface (Shkuratov model). Helfenstein *et al.* (1997) attempted to build a complete model including both SHOE and CBOE on normal surface, but their model contains more parameters than our five data point set.

For clarity below, we refer to "ring particles" as macroscopic, tangible objects in the cm–m range and to "grains" as the individual scatterers making up the regoliths of these particles. The surfaces of the particles can be rough, fractal, faceted, and re-entrant but each surface is itself a regolith composed of grains.

3.1. Hapke Photometric Model

Hapke's model has been used to describe the solar phase curves of many solar system objects. Equations for integral photometry with macroscopic roughness and SHOE have been derived by Hapke (1984, 1986). The five parameters of this model include the grain single-scattering albedo ω_0, and the asymmetry factor g of the grain phase function described by the Henyey–Greenstein phase function $P_{\rm HG}$, the opposition effect sharpness parameter h, the opposition surge amplitude parameter $S(0)$, and the mean macroscopic roughness angle (average surface tilt), $\bar{\theta}$. h is a measurement of the width of the opposition spike and can be related to the particle size distribution and the porosity P within the regolith. Hapke (1986) derived the relation

$$HWHM = 2h = -\frac{3}{4}\ln(P)Y, \tag{1}$$

where Y is a function whose form depends on the particle size distribution. According to this model, *HWHM* should be relatively independent of wavelength. Hapke (1986) defines the total amplitude of the SHOE with the parameter $B_0 = S(0)/\omega_0 P_{\rm HG}(0^\circ)$, where $S(0)$ is defined as the contribution only from first-surface reflections and $\omega_0 P_{\rm HG}(0^\circ)$ is the total amount of backscattered light from a typical regolith particle. Recall that $P_{\rm HG}(0^\circ)$ includes all contributions to the light emerging in the backscatter direction, including internal reflection. For $B_0 = 1$,

all the light is scattered from the first surface. Because the fractional contribution of first-surface reflected light should be smaller for transparent particles than for opaque particles, B_0 is expected to be smaller for higher-albedo (and so transparent) particles, and so should decrease with increasing $\omega_0 P_{\rm HG}(0^\circ)$.

3.2. Drossart Photometric Model

Drossart (1993) calculated the photometric properties of a rough surface described as a mathematical fractal of dimension $D_{\rm H}$ ranging between 2 and 3. For an elementary fractal surface, the expression for the single scattering fractal phase function is given by

$$\Phi_{\rm f}^{\rm s}(\alpha, D_{\rm H}, \omega_0, g) = \mu_{\rm i}\frac{\omega_0}{4} P_{\rm HG}(\alpha, g)\Phi_f(\alpha, D_{\rm H}), \qquad (2)$$

where $\Phi_f(\alpha)$ is a complicated function which describes both the shadowing and diffraction effects on the fractal surface, and $\mu_{\rm i}$ is the effective cosine of incidence angle. $P_{\rm HG}(\alpha, g)$ and ω_0 are, respectively, the Henyey–Greenstein phase function and the single scattering albedo of grains making up the regolith of each element of the fractal surface. In addition to the parameters g and ω_0, Drossart (1993) introduces a fourth parameter $\rho_{\rm H}$ that defines the fraction of projected area toward the observer, which is covered by fractal surface, the rest $(1 - \rho_{\rm H})$ having a "normal" surface described by the standard photometric function for single scattering. $\Phi_{\rm n}^{\rm s}(\alpha, \omega_0, g) = (1 - \rho_{\rm H})\frac{\omega_0}{4}\frac{\mu_{\rm i}}{\mu_{\rm e}+\mu_{\rm i}} P_{\rm HG}(\alpha, g)$, $\mu_{\rm e}$ is the cosine of the emergence angle. An important advantage of this model is that the diffraction, usually neglected in the opposition surge, is taken into account. Drossart (1993) showed that the diffraction could significantly reduce the width of the opposition spike. We extend this model in order to take into account multiple scattering for both the normal surface and the fractal surface as below. The multiple scattering within the "normal" surface can be described by the classical formulation of isotropic multiple scattering, giving $\Phi_{\rm n}^{\rm m} = (1-\rho_{\rm H})\frac{\omega_0}{4}\frac{\mu_{\rm i}}{\mu_{\rm e}+\mu_{\rm i}}[H(\mu_{\rm e})H(\mu_{\rm i})-1]$, where H are the Chandrasekhar H-functions (for e.g., see Hapke 1981). We also add the multiple scattering of the fractal part. The fraction of photons which are absorbed after one scattering event is $(1 - \omega_0)$. The fraction of photons which escape after one scattering event in the fractal surface is $\omega_0 E_{\rm f}$ where $E_{\rm f}$ is given by Drossart (1993, Equation 21). Therefore, the fraction of photons not lost after one scattering is $1 - [(1 - \omega_0) + \omega_0 E_{\rm f}] = \omega_0(1 - E_{\rm f})$. We assume that the multiple diffusion of these photons can be approximated by the formulation of isotropic multiple scattering seen above, so that the multiple scattering by the fractal part can be roughly estimated as $\Phi_{\rm f}^{\rm m} = \rho_{\rm H}(1 - E_{\rm f})\frac{\omega_0^2}{4}\frac{\mu_{\rm i}}{\mu_{\rm e}+\mu_{\rm i}}[H(\mu_{\rm e})H(\mu_{\rm i}) - 1]$. We believe that there are better ways to model the multiple scattering in the fractal surface and also believe that incorporation of shadow illumination by lit facets is tractable, but the fits using this model are so much worse than those for the other two models we studied (Section 4) that we have not attempted these improvements.

By summing up together the expressions of $\Phi_{\rm f}^{\rm s}$, $\Phi_{\rm f}^{\rm m}$, $\Phi_{\rm n}^{\rm s}$, $\Phi_{\rm n}^{\rm m}$, and then by integrating over the disk, we get the integral phase function depending on the four parameters, $D_{\rm H}$, $\rho_{\rm H}$, ω_0, and g.

3.3. Shkuratov Photometric Model

Shkuratov's model includes both coherent backscattering and fractal surfaces, with a semi-empirical treatment of illumination of shadows by illuminated facets (Shkuratov *et al.* 1999). It provides the phase function by employing three parameters: (1) The shadow-hiding effect is described by a parameter $k(\lambda) = k_0(1 - p(\lambda))$, which depends both on the surface albedo p and the surface geometry characteristics through a parameter k_0; the larger the k, the steeper the phase function. k turns out to be a measure of the local macroscopic roughness of the particle's surface; (2) a scatter size d which can be treated as the effective radius of a grain (or the grains); and (3) the diffusion length L of the internally scattered radiation field. L characterizes the attenuation of light from a point source which occurs due to absorption and scattering in the medium, so that L should increase with increasing albedo. The particle phase function normalized to zero phase angle can be written in the form

$$P(\alpha) = B(\alpha) \times S(\alpha), \qquad (3)$$

where the function $B(\alpha)$ describes essentially the shape of the coherent backscattering opposition surge

$$B(\alpha) = \frac{1}{2 + \exp\left(-\frac{d}{L}\right)}\left(2 + \frac{\exp\left(-\frac{d}{L}\right)}{\sqrt{1 + \left(\frac{4\pi L}{\lambda}\sin(\alpha/2)\right)^2}}\right), \qquad (4)$$

and the function $S(\alpha)$[1] the shadowing-effect:

$$S(\alpha) = \frac{2}{\sqrt{\pi}}\exp(-k\alpha)\left(1 - \frac{\alpha}{\pi}\right)\frac{\Gamma\left(\frac{3\pi-\alpha}{2(\pi-\alpha)}\right)}{\Gamma\left(\frac{4\pi-3\alpha}{2(\pi-\alpha)}\right)}. \qquad (5)$$

To give some preliminary indications of the expected effects of the parameters L and d on the shape of the OE, we have performed calculations of two quantities which specify the OE: the half-width at half-maximum *HWHM* and the amplitude of the opposition effect A. The results are shown in Figs. 1 and 2.

For each constant value of d/λ, *HWHM* of the CBOE increases in inverse proportion to L. Because L increases with increasing albedo, the model is consistent with the current theoretical models which predict that the *HWHM* should increase with decreasing particle albedo. We have compared the dependence *HWHM(L)* with the theoretical assertion that *HWHM* is

[1] This function is not valid at large phase angles ($\gtrsim 100^\circ$). A refined model similar to the Shkuratov model corrects this problem (Shkuratov and Helfenstein 2001).

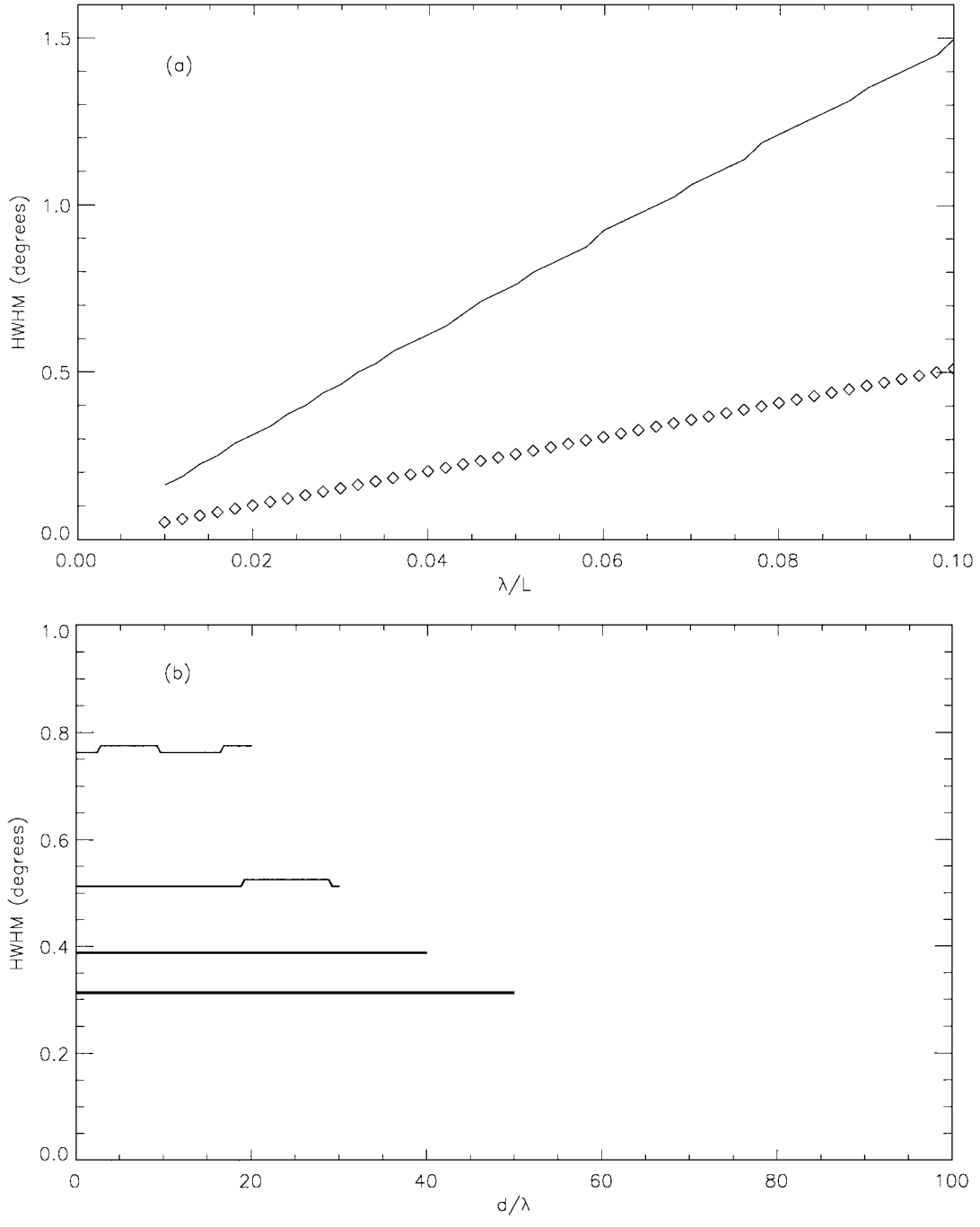

FIG. 1. (a) Half-width at half-maximum of the coherent opposition effect versus the dimensionless parameter L/λ. d/λ is equal to 10. We also plot the theoretical relation given by Eq. (6) (diamond-shaped). (b) *HWHM* is plotted versus d/λ for four values of $L/\lambda = 20$ (thinnest line), 30, 40, and 50 (thickest line). The jumps are due to roundoff errors.

given by (Mishchenko and Dlugach 1993)

$$HWHM \sim \frac{0.6\lambda}{2\pi L_{\rm tr}}, \qquad (6)$$

where $L_{\rm tr}$ is the transport mean free path for photons in the medium. This quantity is the average distance that a photon propagates before its direction is randomized. *HWHM* derived from the Shkuratov model is shown in Fig. 1a. The relation given by Eq. (6) is also plotted in Fig. 1a as diamond-shaped points. From Fig. 1a, one can measure the difference of slope between the two curves. One can then deduce that the diffusion length L of the Shkuratov model is about $30L_{\rm tr}$. The Shkuratov model also predicts that the angular width does not depend on particle size [Eq. (4), Fig. 1b]. While it had been widely accepted that

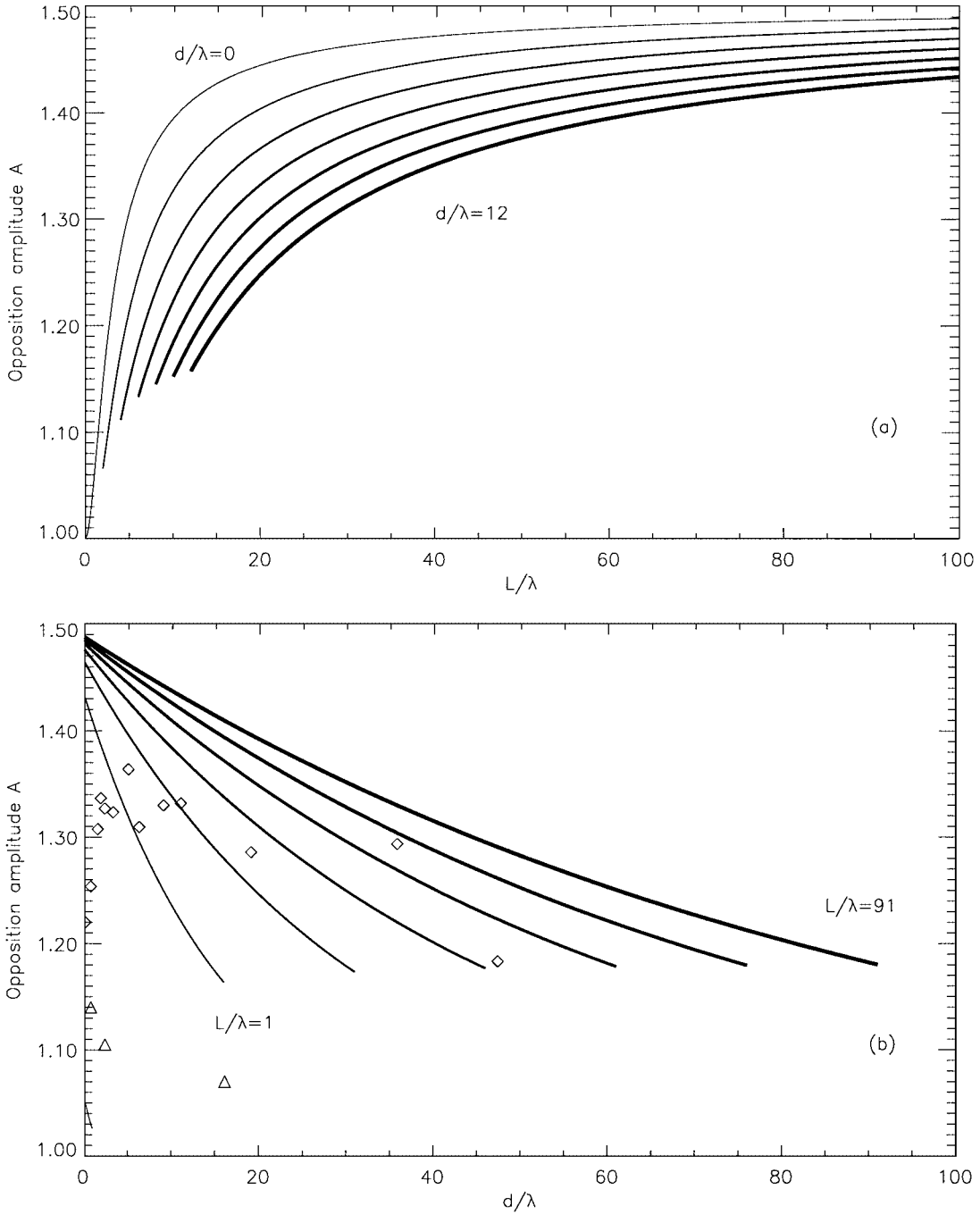

FIG. 2. (a) The amplitude of the opposition effect A versus the dimensionless parameter L/λ for 7 values of d/λ from 0 (thinnest line) to 12 (thickest line). (b) A is plotted versus d/λ for 7 values of L/λ ranged between 1 (thinnest line) to 91 (thickest line) by steps of 15. We compare these behaviors with two published data sets: Diamond-shaped points come from Nelson *et al.* (2000) and triangle points come from Shkuratov *et al.* (1999). Even if the results are quantitatively different, both theoretical and experimental measurements show that A decreases with increasing size. Note the distribution of the Nelson's points is broader than that of Shkuratov's points.

only particles with sizes comparable to the wavelength of light could reproduce the width of CBOE (Mishchenko and Dlugach 1992), new laboratory data show that the dependence of coherent backscatter on grain size is weak at best (Shkuratov *et al.* 1997, Nelson *et al.* 2000).

The second quantity which is studied with the Shkuratov model and compared with laboratory and theoretical results is the OE amplitude A. From Eq. (3), we find $A \sim 1 + \frac{\exp(-\frac{d}{L})}{2}$, implying a maximum of 1.5 when $d \ll L$ (see also Fig. 2a). As expected, the opposition effect is more pronounced with

TABLE II
Regional Amplitude Surges Derived from a Linear–Exponential Fit

	B ring		A ring		Cassini division		C ring	
	0.555 μm	0.336 μm	0.555 μm	0.336 μm	0.555 μm	0.336 μm	0.555 μm	0.336 μm
HWHM (°)	0.47	0.46	0.41	0.41	0.79	0.67	0.67	0.42
A	1.27	1.38	1.27	1.37	1.37	1.39	1.49	1.50

higher values of L for constant grain size d, i.e., with higher values of albedo (Fig. 2a). We point out that this result contradicts the Mishchenko and Dlugach (1992) claim that the amplitude of CBOE could decrease with decreasing absorption. According to these authors, the amplitude can be defined as the fraction $(I_{\text{coherent}} + I_{\text{diffuse}})/I_{\text{diffuse}}$, where I_{diffuse} is the diffuse intensity and I_{coherent} is the coherent contribution. I_{coherent} is much less affected by absorption than I_{diffuse}. Therefore, the observed amplitude of the OE should decrease with increasing albedo.

A strongly decreases with increasing particle size (Fig. 2b). Shkuratov *et al.* (1997, 1999) and Nelson *et al.* (2000) already noted that the opposition peak is more pronounced for the samples of smaller mean particle size. This can be explained by the fact that the number of scatterers per unit area increases with decreasing particle size; an alternative explanation given by Nelson *et al.* (2000) is that this may be due to the effect of irregularities on the surfaces and in the interiors of larger particles, which could act as scattering centers, and to coherent effects that make aggregates of small particles scatter like larger ones. In the context of the Shkuratov model, this should imply that there are more path possibilities to reach L. For values of $d \lesssim \lambda$, the samples of Nelson *et al.* (2000) show that A falls off again. However, the Shkuratov model is not able to reproduce this decrease because it is not suitable for grain size much smaller than λ.

In summary, it is the ratio L/d that tracks the amplitude of the OE. Since the derivation of L depends on *HWHM* only, the value of d will be constrained independently from the observational value of A. This indicates that the grain size can play an important role in the effect of coherent backscattering. In view of these remarks, if the effective grain size of material of lower albedo is smaller than the grain size of higher albedo material, the material of lower albedo can have a bigger OE. Of course, these grain sizes must remain consistent with observed albedos.

4. RESULTS

We present our best fits for each model (Section 4.1), and then we present a comparison between the results of models (Section 4.2). Eventually, our objectives are to evaluate whether the parameters implied are reasonable from a geological point of view and to determine what it is the cause of the opposition surge (Section 4.3).

4.1. Optimal Solutions

In this section, we determine the photometric parameters of three models presented above. A simplex technique is used to find the minimum RMS residual defined as

$$\left[\frac{1}{N}\sum_{i=1}^{N}(P_c(\alpha_i) - P_m(\alpha_i))^2\right]^{1/2},$$

where $P_c(\alpha_i)$ is the calculated phase function at phase angle α_i and $P_m(\alpha_i)$ is the measured phase function at the same phase angle. As shown in Table I, the elevation angles are more or less 10°. But these small differences can affect the brightness. So we correct the brightness by multiplying the profiles by the factor $4\frac{(\mu+\mu')}{\mu}$. We neglect the corrections by the factor

$$\left[1 - \exp\left(\frac{-\tau(\mu+\mu')}{\mu\mu'}\right)\right],$$

because this factor is fairly constant over the data set for optical depth smaller than 1 and because CFD01 showed that the correction factor was imperfect for optical depth larger than 1 (their Fig. 8). To assess the sensitivity of our models to the various phase functions, we have averaged the brightness profiles of large subregions of uniform color of the four main rings (A, B, C rings and Cassini division) at each wavelength.[2] Finally, we used the derived fits to reproduce the color index $C(0.555/0.336)$ of these four main regions which are less affected by the geometry of observations.

4.1.1. Naive fits and interpretations. Because we do not want to bias toward any physical explanation at the moment, a simple four-parameter function is used for approximation of Saturn's ring particles (Piironen *et al.* 2000),

$$f(\alpha) = I_b + z\alpha + I_s \exp(-0.5\alpha/w)\alpha, \tag{7}$$

where I_b and z are the background and the slope of the linear part of the intensity, I_s is the part of the intensity caused by the opposition spike, and w is the width of the spike, In Table II and Fig. 3, we present the derived parameters and the fits, respectively. The backscattering phase curves are characterized by (a) the extreme narrowness of their peak; (b) the

[2] In Section 4.4, we refine our study by presenting an analysis of high-resolution profiles.

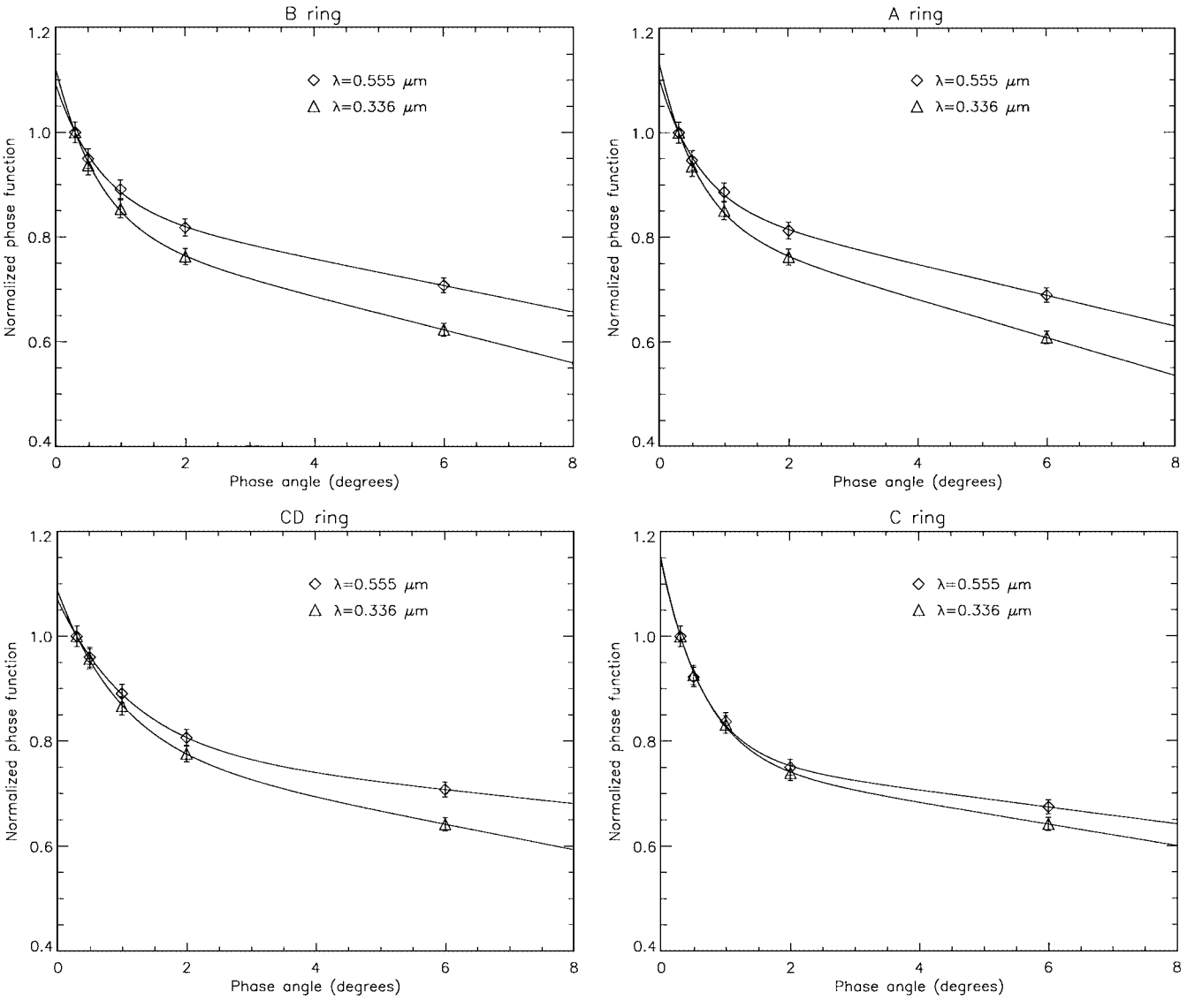

FIG. 3. Phase functions of all the rings compared to their linear-exponential fits (Eq. 7) at two wavelengths.

amplitude at 0.336 μm is almost constant with the albedo of rings; (c) regarding the A and B rings, the amplitude defined as $(I_s + I_b)/I_b$ increases with decreasing albedo and *HWHM*($= 2 \ln 2\ w$) is independent of the wavelength: and (d) *HWHM* strongly varies in the case of the Cassini division and the C ring, and the amplitude is constant with wavelength. The arguments (a) and (b) are weakly in favor of CB. Argument (c) is more consistent with SHOE for the A and B ring particles even when (d) provides support for CB for the lower albedo particles of the Cassini division and the C ring. These ambiguous remarks need further considerations to conclude the cause of the mechanism that produces the opposition spikes of Saturn's ring particles.

4.1.2. Hapke model results. A number of authors have noted that an unique determination of g and $\bar{\theta}$ is extremely difficult from integral phase curves observed in a restricted range of phase angles. The problem is that it is always possible to find a new set of parameters for which the Hapke fonction fits the observational data within the errors. Moreover, g is mostly constrained for small ($\alpha \leq 50^\circ$) and very large phase angles ($\alpha \geq 130^\circ$), while changes in $\bar{\theta}$ affect the shape of the phase curve only at large phase angles (see e.g., Helfenstein *et al.* 1988). Hopefully, we have some knowledge of the scattering properties of particles, such as the geometric albedo p of rings. The derived Hapke parameters can be used to calculate the geometric albedo called $p_{\rm Hapke}$. So, all solutions with geometric albedo within the values of the brightness at 0.3° are considered viable. Constraints are placed on the solutions such that $\bar{\theta}$ is independent of wavelength. According to the shadow-hiding model, the width of the opposition surge h depends primarily on the porosity of the surface and therefore, should also be independent of wavelength.

TABLE III
Photometric Parameters of Hapke Model for B and A Rings

	B ring		A ring	
	0.555 μm	0.336 μm	0.555 μm	0.336 μm
ω_0	0.90 ± 0.07	0.62 ± 0.04	0.75 ± 0.02	0.37 ± 0.05
g	-0.36 ± 0.04	-0.27 ± 0.02	-0.38 ± 0.10	-0.40 ± 0.02
$\bar{\theta}$ (°)	63.7 ± 3.0	63.7 ± 3.0	70.5 ± 4.0	70.5 ± 4.0
$S(0)$	0.77 ± 0.10	0.62 ± 0.08	0.64 ± 0.02	0.64 ± 0.03
h	5.17×10^{-3} $\pm \times 10^{-4}$	5.24×10^{-3} $\pm \times 10^{-4}$	3.40×10^{-3} $\pm 10^{-4}$	3.40×10^{-3} $\pm 10^{-4}$
p_{Hapke}	0.62	0.31	0.51	0.27
p at 0.3°	0.63 ± 0.05	0.31 ± 0.03	0.52 ± 0.07	0.28 ± 0.05
RMS	7.07×10^{-3}	9.48×10^{-3}	6.12×10^{-3}	5.70×10^{-3}

The viable solutions which meet these criteria are listed in Tables III and IV. The errors correspond to all fits with RMS residual less than three times the lowest RMS residual. As shown in Figs. 4 through 7, the Hapke model can give good fits to phase curves. The values of ω_0 are consistent with those of other solar system objects of similar geometric albedo. For instance, at $\lambda = 0.55$ μm, Domingue *et al.* (1991) found $\omega_0 = 0.90 \pm 0.02$ for Rhea ($\omega_0 = 0.90 \pm 0.07$ for the B ring, this work); Helfenstein *et al.* (1988) found $\omega_0 = 0.72 \pm 0.07$ and $\omega_0 = 0.30 \pm 0.03$ for Ariel and Umbriel ($\omega_0 = 0.75 \pm 0.02$ and $\omega_0 = 0.34 \pm 0.02$ for the A ring and the Cassini division). Helfenstein *et al.* (1997) derived $\omega_0 = 0.28 \pm 0.002$ for the lunar "average" terrains ($\omega_0 = 0.28 \pm 0.02$ for the C ring). g is weakly dependent on λ. However, the calculated values of $\bar{\theta}$ for A and B rings are much larger than other values found in the literature. In general, the roughnesses of the icy satellites are described by $\bar{\theta} = 40°$ at most, with an average value of about 20°. In contrast to the A and B rings, the values for the C ring and the Cassini division are consistent with this average value. We reiterate that our low phase angle data are not the most pertinent to constrain the roughness, and a comparison of derived values with roughnesses of other icy surfaces should be taken with caution. However, a comparison between different ring regions can be made with more confidence. So, our results suggest that the C ring and Cassini division particles are smoother than the A and B ring particles. The parameters h and $S(0)$ should be better constrained since our data span angles very close to zero phase angle. The solutions give values of h between 0.003 for the A ring and 0.011 for the Cassini division. h is related to porosity and grain size distribution according to Eq. (1). Figure 8 shows the filling factor $F = (1 - P)$ for different values of the ratio r_l/r_s (r_l and r_s being the largest and smallest particle radii, respectively) and for various power law distributions listed by Hapke (1986). If the size distribution of grains behaves like size distribution of ring particles ($q \sim 3$ from French and Nicholson 2000), the derived porosity is strongly dependent on the ratio r_l/r_s, so that the P can be extremely small or large. By choosing the expression of Y corresponding to a power law index of 4 (value widely used for planetary object surfaces), the values of h yield a porosity ranging between 85% for the Cassini division particles and 99% for the A ring particles. These values are larger than those observed on several atmosphereless satellites. Only Rhea, Europa, and Ariel have similarly porous surfaces (Domingue *et al.* 1991, 1995). Several authors interpret the small value of compaction as the fact that the regolith of the surface is not dominated by meteoritic process, but results from deposition. However, such explanations probably fail for the ring particles which are constantly colliding gently. Furthermore, almost all terrains for which a large value of porosity has been measured have small values of $\bar{\theta}$ in contradiction with the large values of $\bar{\theta}$ we infer for the ring particles.

TABLE IV
Photometric Parameters of Hapke Model for Cassini Division and C Ring

	Cassini division		C ring	
	0.555 μm	0.336 μm	0.555 μm	0.336 μm
ω_0	0.34 ± 0.02	0.13 ± 0.02	0.28 ± 0.02	0.14 ± 0.02
g	-0.34 ± 0.03	-0.44 ± 0.05	-0.26 ± 0.04	-0.31 ± 0.03
$\bar{\theta}$ (°)	10.0 ± 5	10.0 ± 5	26.9 ± 2.0	26.9 ± 2.0
$S(0)$	0.47 ± 0.05	0.41 ± 0.06	0.30 ± 0.06	0.24 ± 0.04
h	1.055×10^{-2} $\pm 5 \times 10^{-4}$	1.110×10^{-2} $\pm 5 \times 10^{-4}$	5.0×10^{-3} 3 ± 10^{-4}	5.2×10^{-3} 3 ± 10^{-4}
p_{Hapke}	0.20	0.13	0.12	0.08
p at 0.3°	0.21 ± 0.05	0.13 ± 0.04	0.13 ± 0.03	0.09 ± 0.02
RMS	3.12×10^{-3}	1.85×10^{-3}	8.24×10^{-3}	7.58×10^{-3}

4.1.3. Drossart model results. As listed in Table V, the RMS residuals of best fits are very bad for all rings. This implies that shadow-hiding alone on hemispherical fractal surfaces cannot reproduce the phase curve of ring particles. However, we believe that this failure is interesting for several reasons: (a) the diffraction on the microstructures of the fractal surface is not able to explain the narrowness of the opposition spike of rings. Actually, this is not a surprising result because Hapke (1999) showed that diffraction effectively does not exist in planetary regoliths. (b) The Drossart model could fit some photometric curves of various Solar System objects which were also well reproduced by the Hapke model (Drossart 1993). This seems to indicate that the CB could play an important role in the Saturn's ring phase curves. (c) One would need to improve the model. The geometric shadowing function and the diffraction contribution was calculated in the case of hemispherical fractal. As pointed out by Drossart (1993), a generalization of this formulation to the case of random fractals could help to describe the properties of regoliths.

Our next modeling shows whether the inclusion of coherent backscatter mechanism produces a significantly better fit to the data.

TABLE V
Photometric Parameters of Drossart Model

	B ring		A ring		Cassini division		C ring	
	0.555 μm	0.336 μm	0.555 μm	0.336 μm	0.555 μm	0.336 μm	0.555 μm	0.336 μm
D_H	3	3	3	3	3	3	3	3
ρ_H	0.75	0.75	0.70	0.70	0.67	0.67	0.58	0.58
ω_0	0.60	0.13	0.35	0.12	0.40	0.15	0.15	0.06
g	0.69	0.69	0.41	0.56	0.34	0.54	0.22	0.06
RMS	0.40	0.69	0.44	0.69	0.44	0.45	0.75	1.42

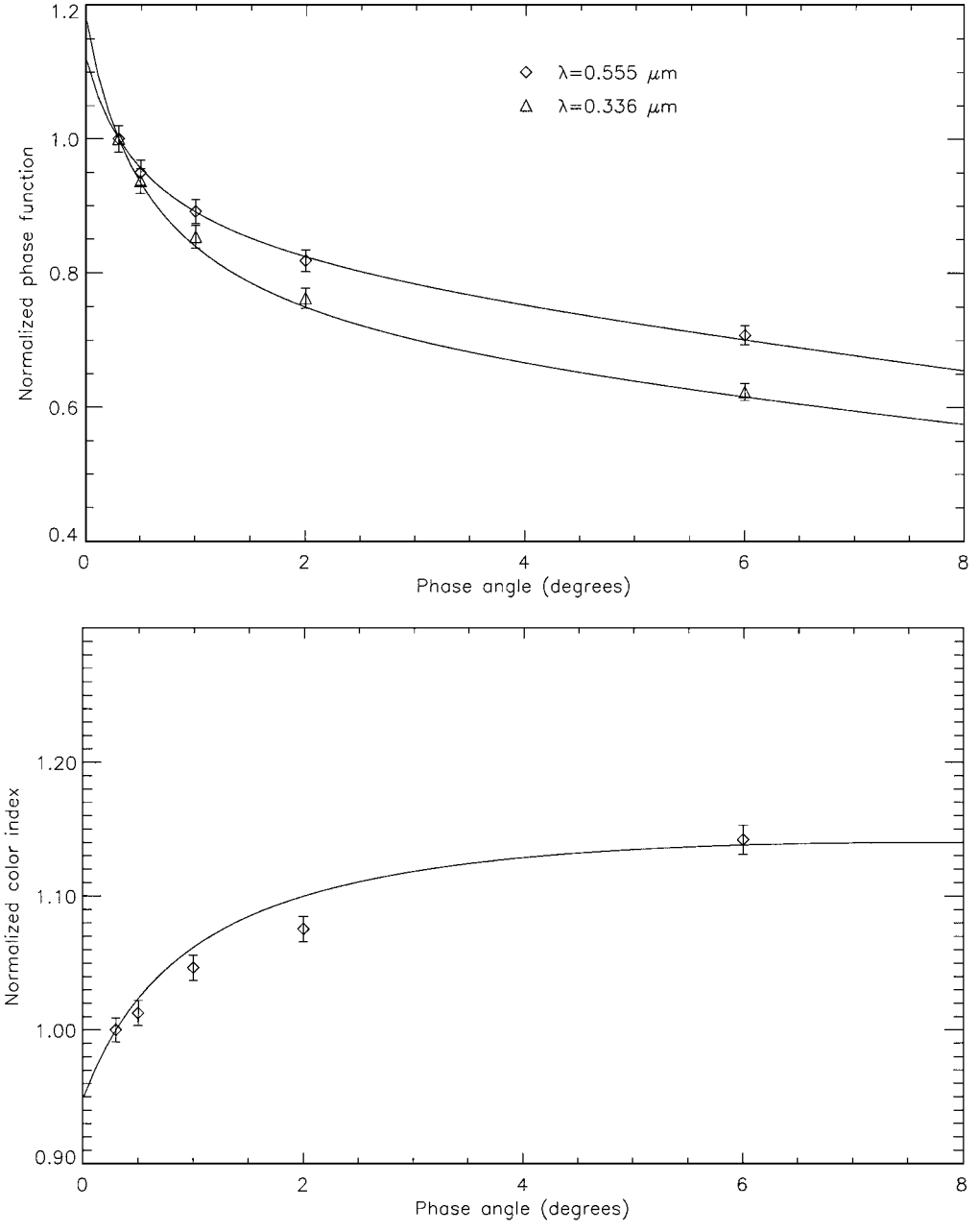

FIG. 4. Upper panel: Comparison of the B ring phase curves at 0.555 μm and 0.336 μm with the Hapke model (solutions 2). The phase curves are normalized at 0.3°. Lower panel: Comparison of the normalized color index $C(0.555/0.336)$ with the Hapke model. The dispersion of ratios across the ring is indicated by the error bars.

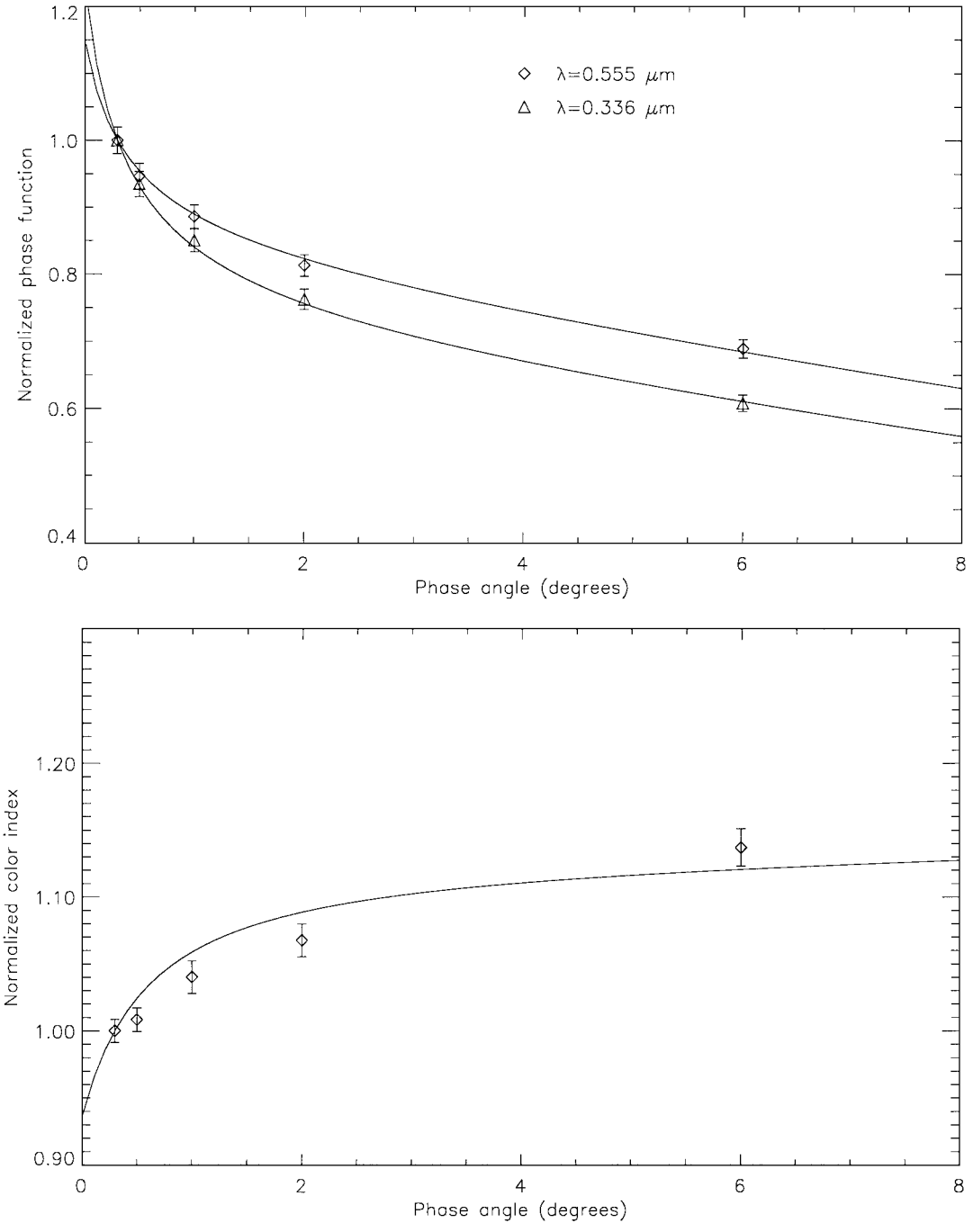

FIG. 5. Hapke model best fits (as in Fig. 4) for the A ring. Note how the color ratio is not well fit.

4.1.4. Shkuratov model results. The parameters are given in Table VI. Figures 9 through 12 show that the Shkuratov model (3 parameters) fits the phase functions well; in fact, the RMS are in average about twice as low as those of Hapke model (five parameters). Within each ring, the "roughness" parameter decreases as wavelength increases. Since the albedo increases with increasing wavelength, the multiple scattering increases leading to smaller k. Moreover, the variations of k are in accordance with the estimation $k = k_0(1 - p)$ within the errors, where k_0 is a function only of surface geometry, which does not depend on albedo (Shkuratov *et al.* 1999). If the surface texture of particles was the same for all rings, we expected that k would decrease with increasing albedo from one ring region to another. In fact, the values of k for the C ring and the Cassini division are smaller than those found for the A and B ring even though the C ring and Cassini division albedos are significantly lower. These results can be best interpreted as a difference of surface texture: the C ring and the Cassini division particles are smoother than the A

TABLE VI
Photometric Parameters of Shkuratov Model

	B ring		A ring		Cassini division		C ring	
	0.555 μm	0.336 μm	0.555 μm	0.336 μm	0.555 μm	0.336 μm	0.555 μm	0.336 μm
k	1.35 ± 0.20	1.85 ± 0.40	1.60 ± 0.30	2.31 ± 0.40	0.50 ± 0.50	1.30 ± 0.60	0.86 ± 0.05	1.31 ± 0.05
d	7.8 ± 1.7	$1.65^{+1.35}_{-0.85}$	8.6 ± 2.7	2.4 ± 1.1	$2.1^{+2.4}_{-1.7}$	$0.9^{+1.6}_{-0.9}$	0.555	0.336
L	$12.7^{+2.5}_{-1.6}$	$7.3^{+2.0}_{-1.0}$	$15.3^{+5.8}_{-3.2}$	$8.5^{+2.7}_{-1.6}$	8.0 ± 1.3	$5.1^{+1.2}_{-0.6}$	15.4 ± 0.2	8.7 ± 0.2
RMS	3.93×10^{-3}	3.23×10^{-3}	3.33×10^{-3}	2.24×10^{-3}	3.0×10^{-3}	4.18×10^{-4}	8.06×10^{-3}	7.07×10^{-3}

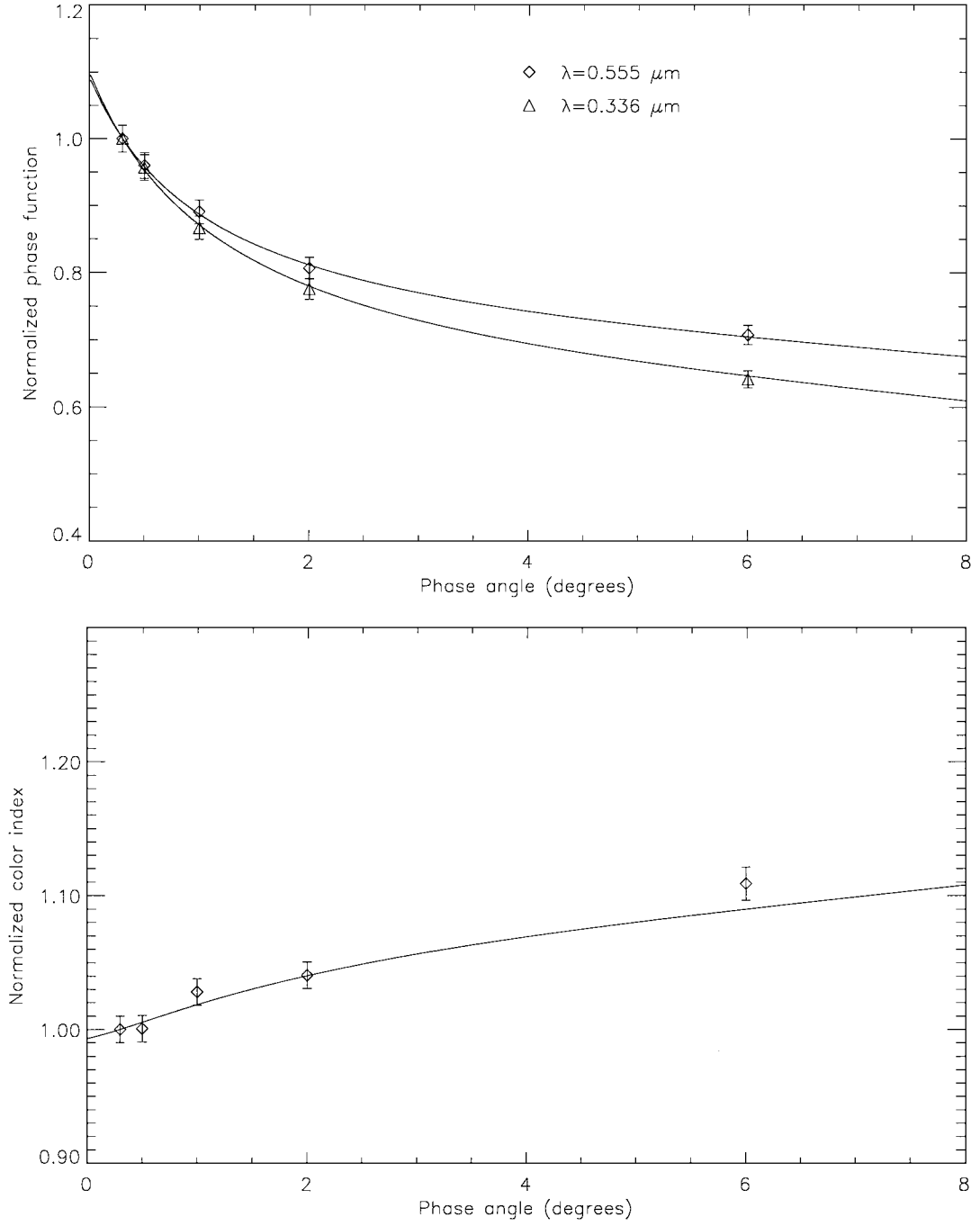

FIG. 6. Hapke model best fits (as in Fig. 4) for the Cassini division.

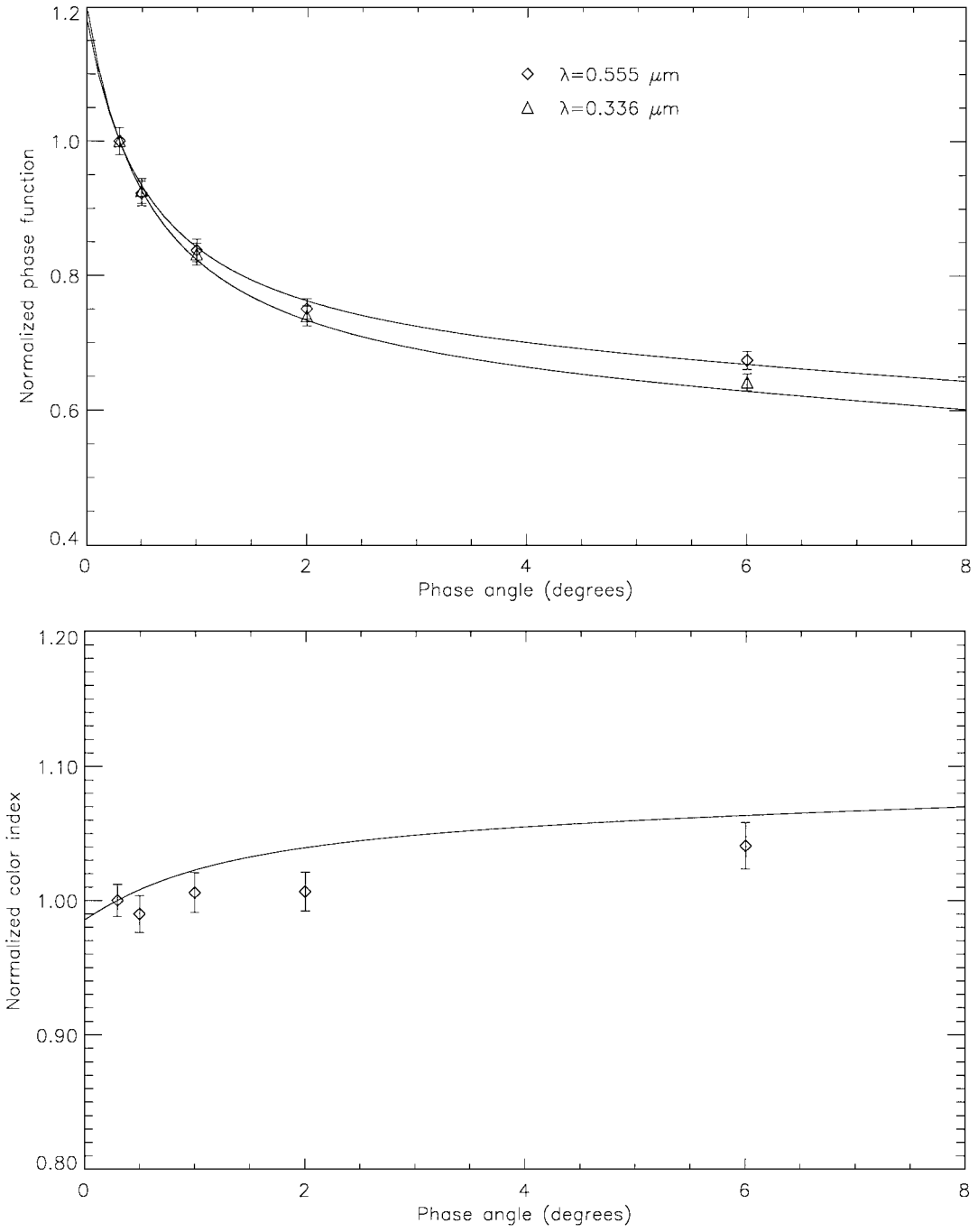

FIG. 7. Hapke model best fits (as in Fig. 4) for the C ring. Note how badly the color ratio is fit here.

and B ring particles. Note that we find again the same conclusion as that obtained with the Hapke modeling.

The solutions give values of L/λ which are roughly constant for each ring (this is primarily from the HWHM of the OE). In other words, the photon transport length is independent of λ, which can be an indication that the surfaces possess quasifractal properties (Shkuratov *et al.* 1999). $L/\lambda \sim 25$ of the C ring is similar to values of the A and B rings, even though albedo and d are lower, but we have no interpretation of this result. The fits give $L/\lambda \sim 15$ for the Cassini division.

Concerning particle size d, the OE of the A and B rings and the Cassini division is consistent with the Shkuratov model for effective grain radii of about 1–10 μm. This result is not in agreement with some previous work: the ice bands in the near-infrared were modeled by regolith grains of about 50-μm radius by Pollack *et al.* (1973) and Clark (1980). However, our result is consistent with more recent reanalyses (Doyle *et al.* 1989, Alix 1998) of the spectra of Clark (1980). In particular, Alix (1998) showed that the near-infrared spectrum and also the position of the H_2O absorption wall between 0.165 and 0.17 μm can be

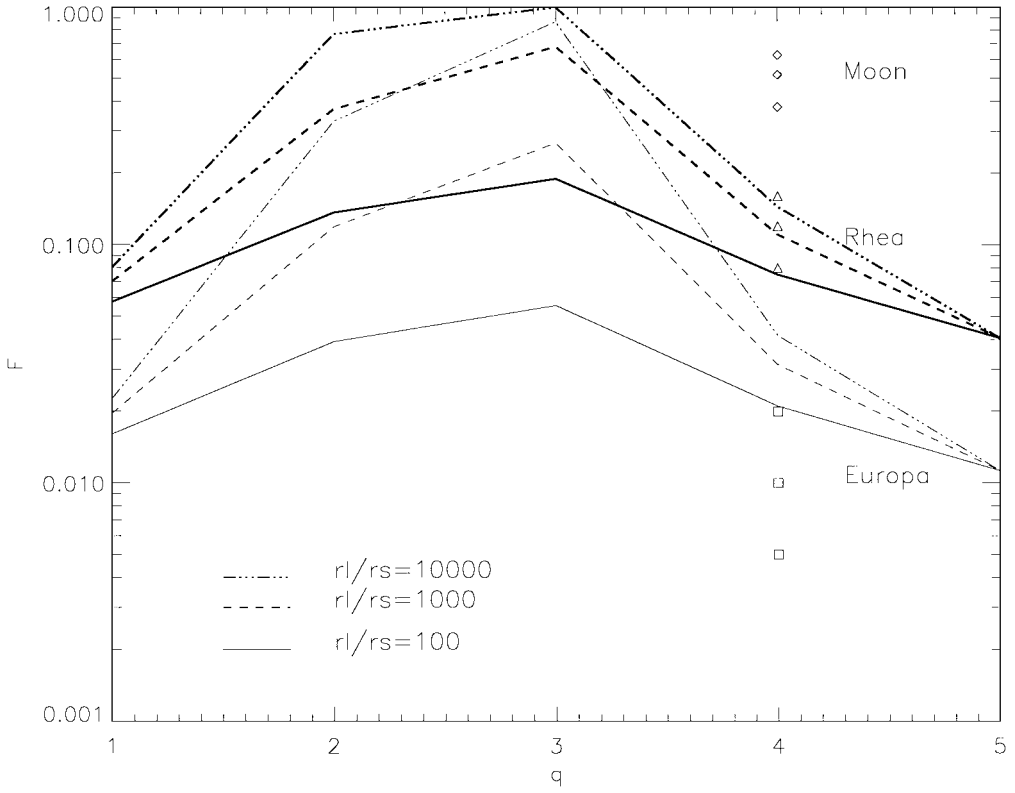

FIG. 8. The filling factor F versus the power-law index of particle size distribution for three values of the ratio r_l/r_s where r_l and r_s are the largest and smallest particle radii respectively. The thick lines (resp. thin lines) represent $h = 0.011$ (resp. $h = 0.003$) corresponding to the h value found for the Cassini Division (resp. A ring).

reproduced by particles of about 1–20 μm radius. We also started the modeling of a composite spectrum from 0.3 to 4.1 μm and found an effective radius of about 25 μm (Poulet and Cuzzi, in preparation). Mishchenko and Dlugach (1992) found a particle size of about 0.1–1 μm, based on their theoretical prediction that the coherent backscatter enhancement is observable only if the particle size is of the order of λ. But recent experimental results (Shkuratov *et al.* 1999, Nelson *et al.* 2000) show in fact a quite different size dependence of CBOE. A typical signature of observed coherent backscatter is that it is only weakly dependent on particle size and that a surface with smaller particles has a stronger peak. Our modeling gives d smaller in U than in V because the amplitude of the CB opposition surge is stronger in U (Fig. 9 through 12). This wavelength-dependent effective grain size, also observed (but not interpreted) in the case of the Moon (Shkuratov *et al.* 1999) will be analyzed in Section 4.3. For the C ring, the best fits are obtained with $d = 0$. However, such a value has no physical sense, so that we consider viable solutions by taking d on the order of λ. Note that the RMS of such solutions are about three times larger than the best fits obtained with $d = 0$. The case $d \sim \lambda$ implies structures on all length scales, with the wavelength merely selecting structures comparable to itself. By comparison, the unambiguous result that $d \gg \lambda$ could mean fewer cracks, small scattering centers, or asperities on smoother grains.

To estimate relative contributions of the shadow-hiding and coherent backscattering enhancement effects, we omitted the interference multiplier in Eq. (3) and then calculated the pure shadowing part. The results, presented in Fig. 9 through 12 by dashed lines, show that the SHOE as defined by the Shkuratov model[3] is incapable of producing the opposition surge. The contribution of coherent backscattering is only a few percent at $\alpha = 6.0^\circ$, but reaches almost 10 percent at $\alpha = 2.0^\circ$.

4.2. Color Ratio C(0.555/0.336)

In the previous sections, we have examined the various solutions given by the Hapke model and the Shkuratov model. Both fit the observed phase functions almost equally well with parameters which are physically "realistic" (even if some Hapke parameters are a little bit extreme). Thus, we need to do further investigations to test the models. The color index is useful to achieve that, because it is less affected by the geometry of observations. CFD01 noted that the phase reddening of rings between 2° and 6° was slightly larger than that of other icy surfaces. The phase dependence of the spectral ratio is better

[3] The Shkuratov model puts all the narrow-backscatter-peak parts into his CB function. On the other hand, the Hapke model has a porosity-related shadowing function which contributes to the OE.

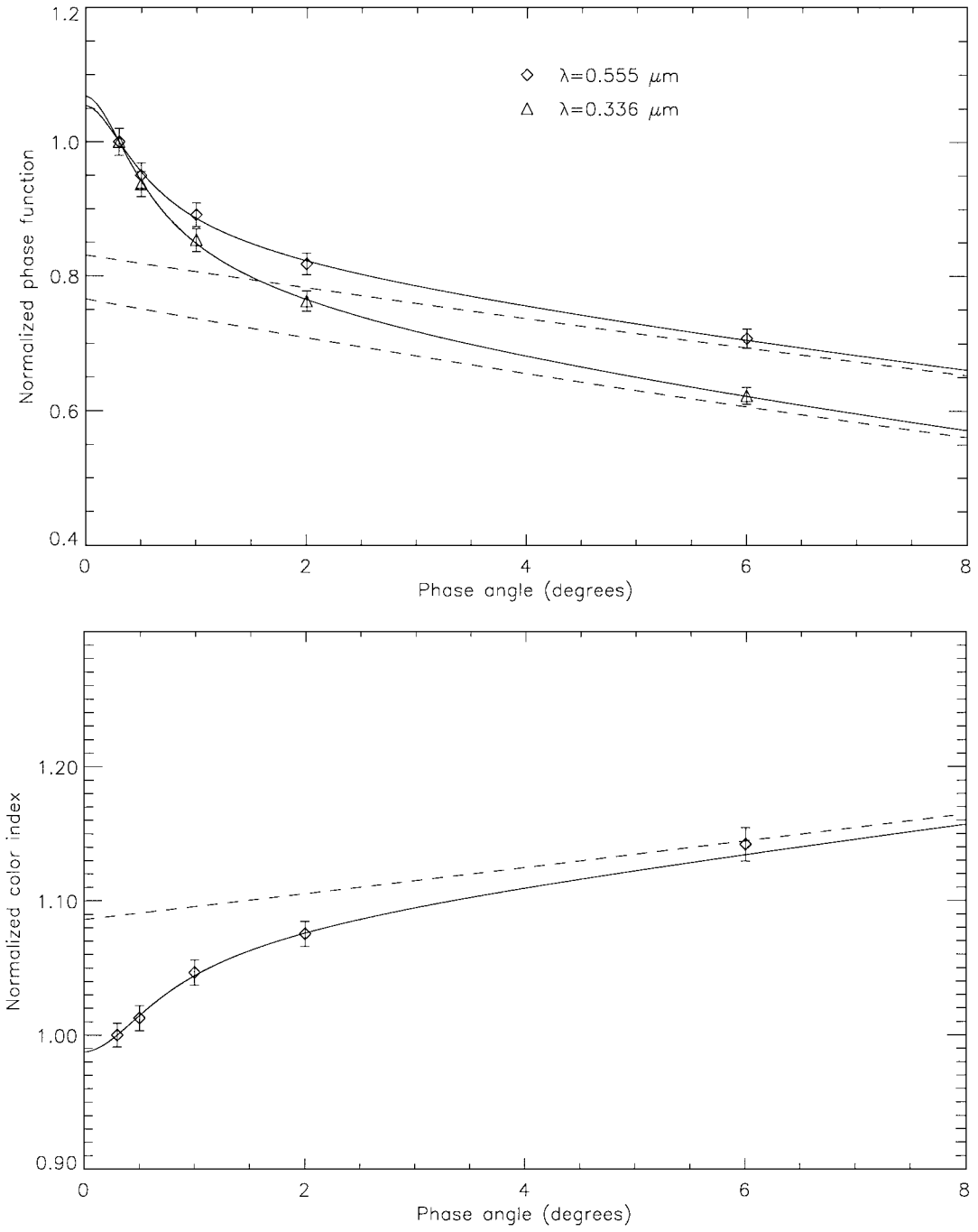

FIG. 9. Upper panel: Comparison of the B ring phase curves at 0.555 μm and 0.336 μm with the Shkuratov model. The phase curves are normalized at 0.3°. The dashed line corresponds to the pure shadow-hiding component. Lower panel: Comparison of the normalized color index $C(0.555/0.336)$ with the Shkuratov model. The dashed line corresponds to the pure shadow-hiding component.

reproduced by the Shkuratov model (Figs. 9 through 12) than by the Hapke model (Figs. 4 through 7). Hapke modeling does not reproduce the reddening of the A and B rings well, while the Shkuratov fits are very good for all the rings. In Hapke theory, multiple scattering between surface facets is neglected. For the fairly red B and A rings, the increase of the index $C(0.555/0.336)$ with α between 2° and 6° is larger than for more neutral regions as the C ring and the Cassini division. Therefore, the Hapke model needs to treat it as a regolith multiple scattering effect. The semi-empirical treatment of the Shkuratov model includes the interfacet multiple scattering, whose effect increases with increasing α. Therefore, the strong phase dependence of the brightness and color can be attributable to the fact that the albedo (and so the contribution of interfacet multiple scattering) of the bright and colored particles is greater precisely in red rays. In other words, the shadows are illuminated

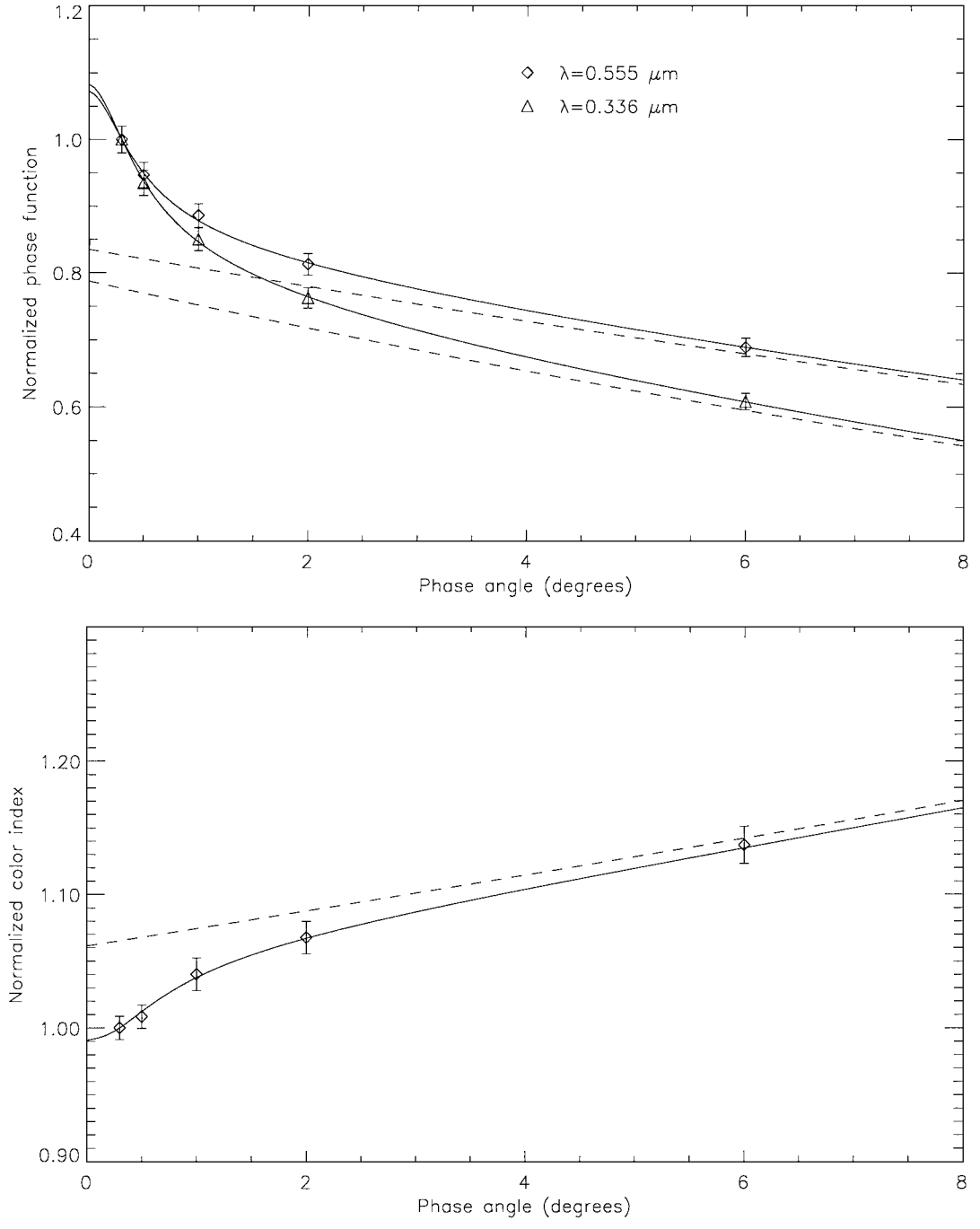

FIG. 10. Shkuratov model best fits (as in Fig. 9) for the A ring.

by multiple interfacet scattering. This effect can be expressed in terms of Eq. (3). For instance, by taking a ratio L/λ roughly constant and $d \sim \lambda$ (parameters for the C ring and Cassini division particles within errors), the behavior of the $C(0.555/0.336)$ is mainly proportional to $\exp[(k_{0.336} - k_{0.555})\alpha]$ as shown in the dashed line in Fig. 12 ($k_{0.555}$ and $k_{0.336}$ are the coefficient k in 0.555 and 0.336, respectively). For the A and B rings, d/λ is not constant, so their color ratio is less well reproduced by $\exp[(k_{0.336} - k_{0.555})\alpha]$.

At small phase angles, this explanation fails. The reddening varies more strongly between $\alpha = 2^\circ$ and 0.5° than at large α, and then the slope flattens between $\alpha = 0.5^\circ$ and 0.3°. At very small α, the C ring seems to exhibit an anomalous phase dependence (Fig. 12): the color ratio, after decreasing down to $\alpha \sim 0.5^\circ$, even seems to increase between 0.5° and 0.3° phase. Recall that the "error bars" shown in these figures are not uncertainties in the measurements from one phase angle to another, but represent the envelope of variation across each ring region. According

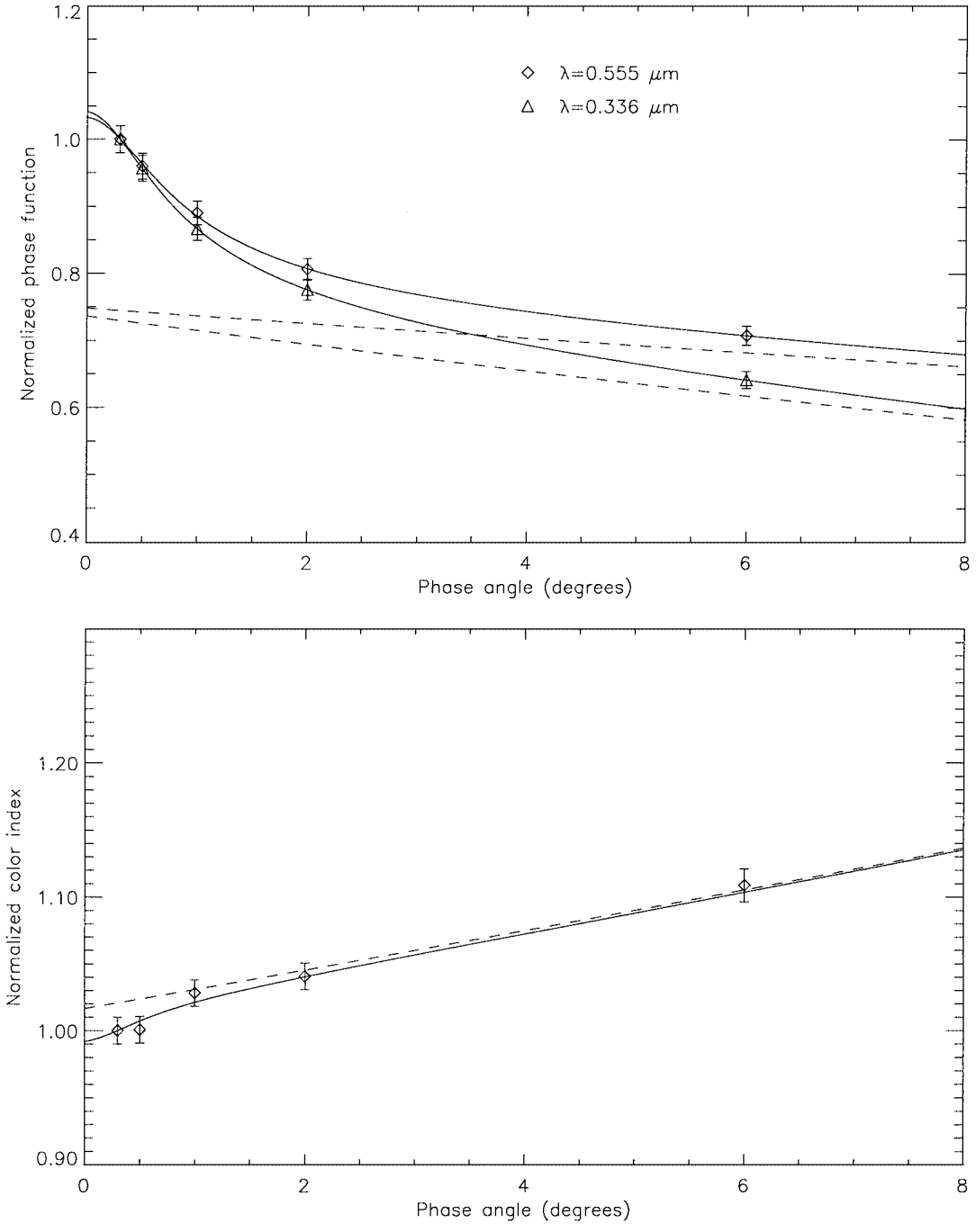

FIG. 11. Shkuratov model best fits (as in Fig. 9) for the Cassini division.

to the theory of shadow-hiding, the color ratio should decrease with decreasing phase angle. We can reproduce this trend in the theoretical Hapke color ratios for $\alpha < 0.3^\circ$ (Figs. 4 through 7), but the fits are not really very good. In contrast, an increase of the color index with decreasing phase angle can also be explained in terms of the mechanism of coherent backscattering (Shkuratov *et al.* 1996, 1999). At very small phase angles, the phase function in the V light becomes steeper than in the U light because of the increasing relative contribution from coherent backscattering.

In summary, we find that the Shkuratov model, which includes a combination of multiple regolith grain scattering, coherent backscattering, and shadow-hiding effects can represent the overall increase of $C(0.555/0.336)$ with α much better than can the Hapke model, using fewer free parameters and without requiring parameters which are in contradiction with independent expectations (high porosity, very strong roughness). Moreover, the coherent backscattering provides a mechanism to explain the anomalous opposition reddening at phase angle lower than

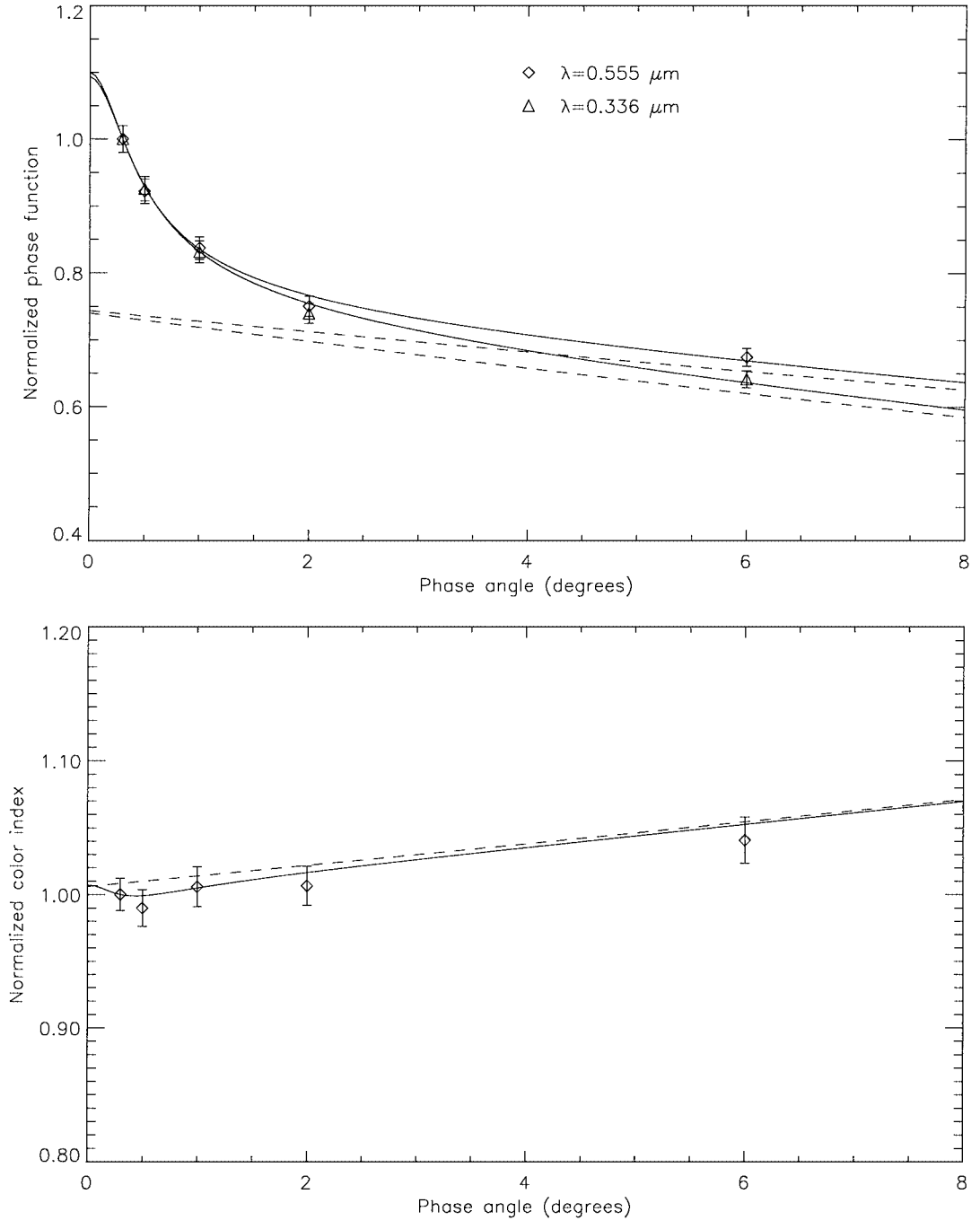

FIG. 12. Shkuratov model best fits (as in Fig. 9) for the C ring.

0.5°, while the shadow-effect modeled by Hapke theory cannot produce opposition reddening at all. Therefore, regarding the phase color effect, the detailed fits of the CB effect in the Shkuratov model are noticeably better than the SH effect in the Hapke model.

4.3. Opposition Surge Behavior of Four Main Rings

Even though the previous paragraph showed that the CB seems to dominate the opposition surge of all of Saturn's main rings, there are still open questions. Why is this effect more pronounced for the C ring and the Cassini division than for the A and B rings? Why is the amplitude of the opposition effect larger at 0.336 μm than at 0.555 μm? A simple explanation for the CBOE would be that it would be stronger in higher albedo surfaces. In this section, we examine more carefully the properties of the opposition surge by examining both the phase function and the color ratio in order to be more confident about the identification of the mechanism responsible of the OE and also to deduce other properties of the regolith.

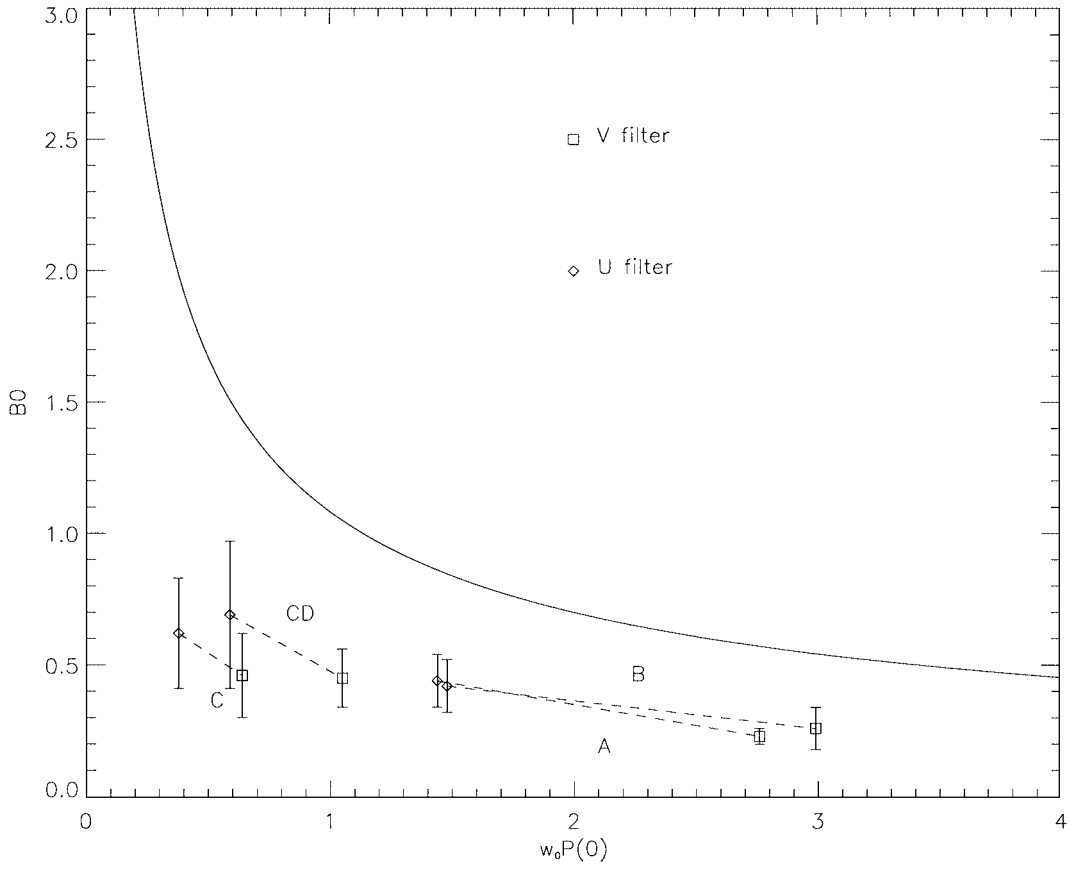

FIG. 13. Hapke parameter B_0 versus $\omega_0 P_{HG}(0^\circ)$ from the Hapke modeling. The solid line is the behavior predicted from a survey of the opposition surge amplitude for other solar system objects whose phase curves were derived by using the Hapke theory (Helfenstein *et al.* 1997). This empirical relation is $B_0 = 1.083[\omega_0 P_{HG}(0^\circ)]^{-0.629}$.

Another test to reject the SHOE unambiguously is to present the trend of the total amplitude of SHOE B_0 relative to $S(0)/\omega_0 P_{HG}(0^\circ)$. Figure 13 shows that the observed trend of amplitude B_0 is independent of $S(0)/\omega_0 P_{HG}(0^\circ)$. This behavior is not consistent with the SHOE, which predicts a strong decrease of the amplitude with increasing albedo.

According to the mechanism of coherent backscattering, more reflective material should exhibit stronger opposition surge amplitudes than should less reflective material. However, our measurements of the relative strength of opposition surges derived from the Shkuratov model show an opposite trend (Table VII): a decrease with increasing both wavelength and albedo. We shall demonstrate below that this effect can be explained at least qualitatively consistent with CB being the physical phenomenon that contributes to the opposition behavior. In fact, this phenomenon can be interpreted as typical of the coherent backscatter origin of the opposition effect according to Shkuratov *et al.* (1999). As shown in Fig. 2, A depends on two quantities: the grain albedo through L and the effective size parameter d. A increases with increasing L but decreases with increasing d. Even though the data show a weaker effect than the theory, both new laboratory data and the Shkuratov model show that samples with smaller particles have a stronger OE. So, a smaller effective size parameter can compensate for a smaller albedo, leading to a bigger opposition surge for lower albedo material. From Table VI, we remark indeed that the

TABLE VII
Regional Amplitude Surges Derived from Shkuratov Model

	B ring		A ring		Cassini division		C ring	
	0.555 μm	0.336 μm	0.555 μm	0.336 μm	0.555 μm	0.336 μm	0.555 μm	0.336 μm
HWHM (°)	0.67 ± 0.11	0.71 ± 0.15	0.56 ± 0.17	0.62 ± 0.15	1.04 ± 0.20	1.02 ± 0.22	0.58 ± 0.04	0.63 ± 0.04
A	1.50 ± 0.03	1.77 ± 0.02	1.55 ± 0.03	1.80 ± 0.02	1.45 ± 0.11	1.65 ± 0.10	1.62 ± 0.03	1.72 ± 0.03

TABLE VIII
Power-Law Index q of Size Distributions

	B ring	A ring	Cassini division	C ring
a	0.01	0.0125	0.016	0.011
b	1.44	1.46	1.43	1.44
q	3.20 ± 0.04	3.10 ± 0.04	$3.05^{+0.30}_{-0.04}$	$3.02^{+0.05}_{-0.01}$

fitted values of d for A and B rings are larger than for the C ring.

The fact that the surge amplitude A increases with decreasing λ (decreasing particle albedo) can also be explained in terms of particle-size difference. Since A increases as d/λ decreases with a maximum for $d \sim \lambda$, the amplitude will depend on the number of scatterers per unit area of size smaller than a few λ. The surface of a particle should be covered by particles of different sizes. The fitted values of d decrease with λ for the B and A rings and the Cassini division; as shown below, this indicates that the particles of size similar to $\lambda = 0.336$ μm are much more numerous than particles of size comparable to $\lambda = 0.555$ μm.

The ratio of the amplitudes at $\lambda = 0.555$ μm and $\lambda = 0.336$ μm can be used to estimate the size distribution of particles. To describe the radius distribution of the grains, we use a power-law distribution of grains per unit area with q referred to as the power-law index $n(d) = n_0 d^{-q}$. From Fig. 2b, we model the dependence of A on d/λ as a linear function: $A(d/\lambda) \sim -a\frac{d}{\lambda} + b$ with the size d ranged between $x_{\min}\lambda$ and $x_{\max}\lambda$. The coefficients $x_{\min}$ and $x_{\max}$ are equal to 0.1 and 20, respectively. Table VIII gives the values of the coefficient a and b for each value L/λ corresponding to a ring. For $q > 3$, the amplitude of the OE should be proportional to

$$A(\lambda) \sim \int_{x_{\min}\lambda}^{x_{\max}\lambda} \pi d^2 d^{-q}\left(-a\frac{d}{\lambda} + b\right)\mathrm{d}d \sim \frac{C(q, a, b, x_{\min}, x_{\max})}{\lambda^{q-3}}. \quad (8)$$

C is a constant which must be positive to make $A(\lambda)$ decreasing. In practice, this condition is always checked. By comparing the ratio of the surge amplitude at two studied wavelengths $A(0.555)/A(0.336)$ using Eq. (8) with the values given in Table VII, we can give an estimate of q as between 3 and 3.2 (Table VIII).

Equations (3)–(5) can be used to understand why only the C ring exhibits the anomalous OE. Since $d/\lambda \ll 1$ for the C ring, these three equations can be rearranged to express the ratio $C(0.555/0.336)$ as

$$C(0.555/0.336) \sim \frac{2 + \frac{1}{\sqrt{1+\left(\frac{4\pi L_{0.5}}{\lambda_{0.5}}\sin(\alpha/2)\right)^2}}}{2 + \frac{1}{\sqrt{1+\left(\frac{4\pi L_{0.3}}{\lambda_{0.3}}\sin(\alpha/2)\right)^2}}} \exp[(k_{0.3} - k_{0.5})\alpha], \quad (9)$$

where the indices 0.3 and 0.5 refer to the wavelengths of 0.336 μm and 0.555 μm, respectively.

If $k_{0.3} > k_{0.5}$, the pure shadow-hiding contribution (second term on right-hand side of Eq. (9)) increases with increasing α, leading to a growth of $C(0.555/0.336)$. A minimum at small phase angles arises for the rings because $C(0.555/0.336)$ is equal to 1 at 0° and the contribution due to the reddened shadows increases with increasing α. The first term on the right-hand side of Eq. (9) is the coherent backscattering contribution. It affects the value of C mainly at small phase angles. If $L_{0.3} > \frac{\lambda_{0.3}}{\lambda_{0.5}} L_{0.5} \gtrsim 0.6 L_{0.5}$, then this contribution is always larger than 1 and the color ratio C increases monotonically as in the A and B rings and the Cassini division. In contrast, if $L_{0.3} < \frac{\lambda_{0.3}}{\lambda_{0.5}} L_{0.5} \gtrsim 0.6 L_{0.5}$, then the CB contribution to the color ratio is smaller than 1, and C initially decreases due to the CB contribution before rising due to the shadow illumination effect. Such an effect is observed for the C ring, because $L_{0.3}$ is smaller than $0.6 L_{0.5}$. In other words, the phase angle where the minimum occurs depends on the widths of the OE at two wavelengths. This width-dependence of the color index can lead to a large variety of forms of the OE of color. We believe it is easier to detect the anomalous OE (color minimum for $\alpha > 0°$) for neutral and smooth material (as in the C ring) than it is for red and rough material, because the contribution of the pure shadow-hiding overwhelms the smaller CBOE effect. Actually, it is not excluded that the other rings have an anomalous OE of color at very small phase angles because the decrease of color index between 0.5° and 0.3° is significantly smaller than is the decrease between 2° and 0.5°.

In summary, the presence of coherent backscatter appears to be indicated by the following:

- The observational data (both phase curves and color ratio) are well reproduced by a model which includes this mechanism.
- The extreme narrowness (less than 1°) of the peaks.
- The fact that the amplitude A in the visible is larger than unity for all the rings, and in particular for the high albedo B ring where shadow-hiding should be most likely to be negligible. Without CBOE, the amplitude should be closer to unity for the B ring particles with $\omega_0 \sim 0.6$, because multiply-scattered light would almost completely fill in shadows cast by particles.
- The constant opposition surge amplitude A with increasing albedos (Fig. 13) which is inconsistent with the SHOE in the context of Hapke model, but can be modeled as grain size effects compensating albedo effects in terms of the CBOE.
- The fact that the color ratio of the C ring exhibits a minimum at small phase angle. As far as we know, this effect can be explained only in terms of the coherent enhancement of backscattering.

We have to admit that the discrepancies between SHOE and CBOE are far from settled and the five arguments presented above are only weakly in favor of CBOE. There is also the probability that, in the case of C ring, shadowing may contribute to the opposition spike. Based on some recent experiments, we

found that the grain size effect could cancel the albedo effect, but we need a rigourous computation for a scattering surface with a distribution of particle sizes to confirm this effect. Moreover, we use the Shkuratov model, which neglects the effects of particle shape that could be significant on the mechanism of CB. Finally, the difficulty with the Shkuratov model is that it is semi-empirical and derivated from intuitive arguments rather than from physical principles. In particular, the parameters d and L are not clearly defined.

4.4. Regional Surface Structure

We use the Shkuratov model to produce high-resolution radial profiles (uniformly spaced at 100 km) of adjusted parameters at two wavelengths (Fig. 14). To estimate the quality of fits, we plot in the lowest panel the postfit root–mean–square residual. There are large values of RMS in the C ring, near the inner edge of the B ring, and in the Cassini division, due to some artifacts produced near sharp edges by the wavelength dependence of the HST point spread function (CFD01). Otherwise, the RMS are of the order of those found for the averaged rings.

4.4.1. Effective regolith particle size. The upper panel of Fig. 14 shows the profile of the effective particle size d at two wavelengths. The values are consistent with the values found for the averaged profiles, i.e., $d \sim 1$–10 μm for the A and B rings and $d \sim \lambda$ for the C ring. It must be emphasized that the best fits for the C ring phase function is obtained for $d = 0$ μm, even though such a value would correspond to an overextension of the Shkuratov theory. Actually, it may be that the opposition

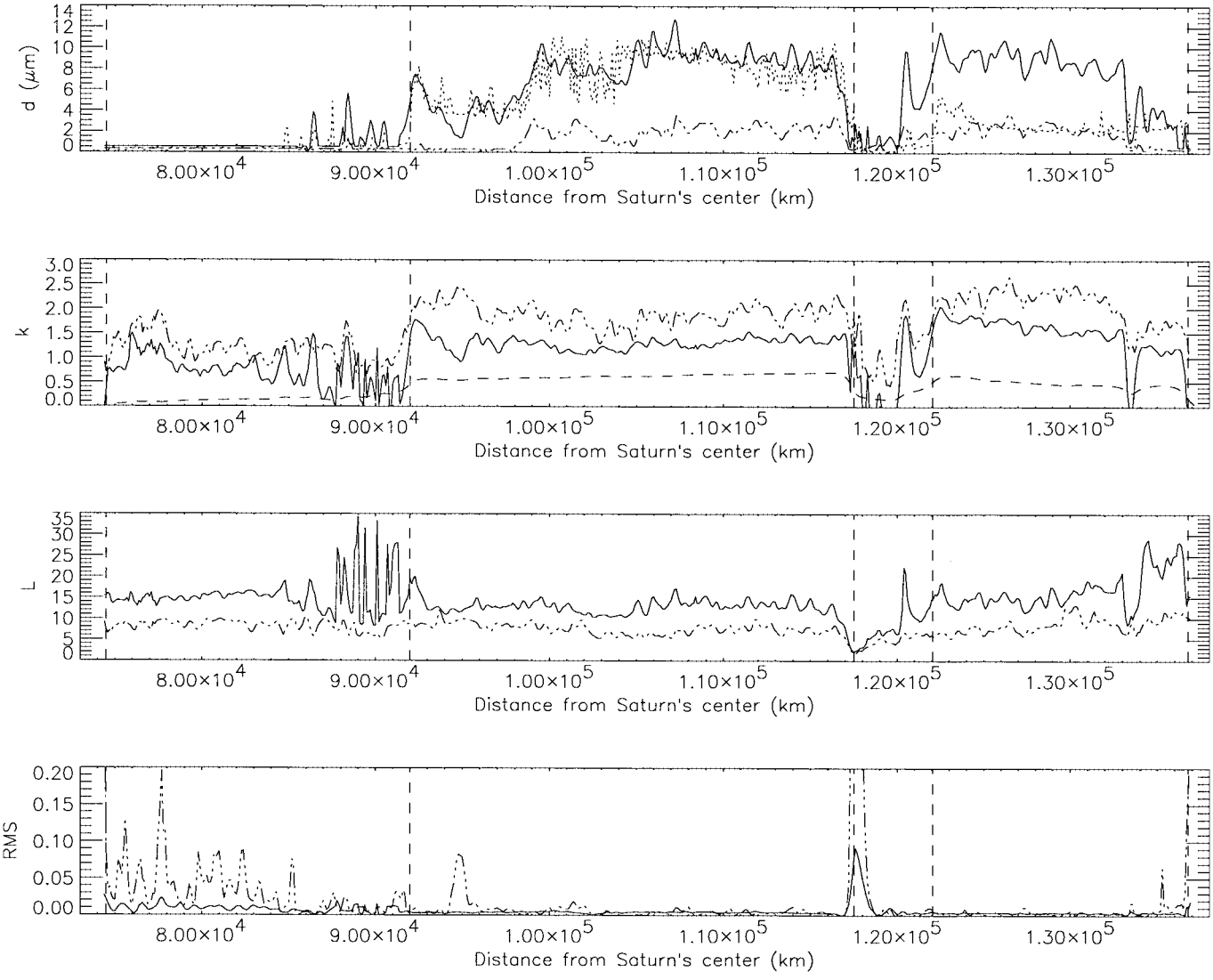

FIG. 14. Radial profiles of adjusted parameters d, k and L at $\lambda = 0.555$ μm (continuous line) and $\lambda = 0.336$ μm (dotted-dashed line). The RMS is plotted in the bottom panel. In the d panel (upper panel), the normalized Voyager PPS optical depth profile is shown in the dotted line. In the opaque central region of the B ring, the PPS observations have very low SNR and provide only a lower limit to the optical depth (French and Nicholson 2000), so that the correlation of d with τ is not as strong as suggested by the figure. In the k panel, the dashed line defines the geometric albedo at $\lambda = 0.555$ μm at $\alpha = 0.3°$.

effect amplitude in the C ring, where the particles are darker, relies partly on some contribution to the SHOE (which is not modeled by the Shkuratov theory; see Section 4.1.4).

In contrast to the broader ring regions, it is difficult to set tight constraints on effective particle size of the Cassini division because it is narrow and it is affected by the PSF's artifacts. Nevertheless, it seems that d is smaller in the Cassini division than in the A and B rings. An overall correlation exists between d and the PPS optical depth τ (plotted as a dotted line). At large scale (10^4 km), the larger the optical depth, the larger the particle effective size. Even at smaller scales (10^3 km), the correlation is strong in the B ring. In the inner B ring, typical regolith particles are smaller than in the opaque central region of the B ring (100,000–110,000 km), where $d \sim 7$–10 μm. Spokes are more frequent in the mid and outer B ring, but the spoke particles themselves are much smaller, $d \sim 0.6\,\mu\text{m} \pm 0.2$ (Doyle and Grün 1990). The uniformity of the outer B ring is found again in the A ring interior to the Encke division. The production of microscopic particles should result from collisions between ring particles and meteoritic erosion. It may be possible that the less frequent but stronger collisions in the lower optical depth rings could lead to the creation of more abundant small particles. Our modeling also hints that there is a greater abundance of small particles in the outer A ring, even though the optical depth increases there—apparently in conflict with this hypothesis. However, the plethora of density and bending waves in this region should result in larger relative velocities in this region and consequently the creation of small particles.

4.4.2. Roughness. For a given ring, $k_{0.336}$ is larger than $k_{0.555}$ by an amount consistent with relative geometric albedos (Section 4.1.4). k is larger for the B and A rings than for the Cassini division and the C ring, incompatible with an albedo effect and implying that the B and A ring particles are rougher. The roughness is nearly uniform within the B ring. Some apparent radial variations of about 1000–1500 km width are not the same at two wavelengths, so we believe that they correspond to the errors of measurements. In contrast, k values of the inner and middle A ring are markedly larger than that of particles of the outer A ring, consistent with the albedo and the smoothness increases from the inner edge to the outer edge as found by Dones *et al.* (1993). In summary, the modeling supports a τ-dependence of particle roughness with the trend that the particles in smaller optical depth regions are significantly smoother, presumably due to the dominance of collisional compaction over transient clustering.

The recent Shkuratov model has not been used widely for the analysis of phase curves of other atmosphereless bodies. Shkuratov *et al.* (1999) found $k = 0.86$ and $k = 1.31$ for the Moon at $\lambda \sim 0.55$ μm and $\lambda \sim 0.36$ μm. These values are roughly consistent with those of the C ring and the Cassini division. In contrast, the A and B ring particles, whose albedo is much larger than that of the Moon, seem to be much rougher. Such unusual roughness suggests that the particles are lumpy, aggregate particles, which confirms other works supporting also the aggregate form in dense rings (Weidenschilling *et al.* 1984. Longaretti 1989, Rosen *et al.* 1991, Salo 1992, Richardson 1994).

5. CONCLUSION AND FUTURE WORK

HST observations of Saturn's rings reveal that the coherent backscatter opposition effect may mainly contribute to the photometric behavior of Saturn's ring particles near opposition. Also, an apparent anomalous effect of the color index may have been detected for the C ring, which can only be explained by coherent backscattering. In the context of the Shkuratov model, the strength of the opposition effect depends primarily on the regolith grain size, which we then find to vary systematically in a way that correlates with local optical depth. The opposition surge is the largest for the C ring particles; in the Shkuratov theory, this implies the effective size of regolith particles is comparable to λ. There is a τ-dependence of the effective size, which is unexplained, but may derive from the stronger collision velocity in the regions of lower τ leading to the creation of more abundant small particles. Assuming a power law size distribution for regolith particles, we found a power law index between 3 and 3.2. We point out that these size distributions are compatible with collisional and disruptive processes. However, as we pointed out in Sections 2.2 and 3.3, conclusions should be drawn cautiously because (1) the discrepancies between SHOE and CBOE for a scattering surface with a distribution of particle sizes or partially absorbing materials are far from settled; (2) some laboratory measurements do not agree with the theoretical results; (3) one uses to compare the integrated brightness of planetary objects with the surface brightness of laboratory targets, which are obviously very different in terms of size scale.; (4) numerous laboratory experiments and theoretical considerations have shown strong dependence of phase function on surface roughness, particle shape, and size particles.

For phase angles larger than 2°, the phase function of individual particles is still wavelength-dependent, giving a pronounced phase dependence of color which is especially strong for the brighter, redder A and B rings. In the context of the Shkuratov model, illuminated facets are brighter at 0.555 μm than at 0.336 μm and more effectively illuminate the shadows, which are more visible as α increases. Furthermore, both Hapke and Shkuratov models provide essentially the same conclusion, namely that the A and B ring particles are dramatically rougher than those of the Moon or the C ring particles. These findings support a model of lumpy particle structure in the A and B rings, constructed as aggregates of macroscopic aggregates, with many re-entrant surfaces with deep shadows which become illuminated by multiple facet reflections as α increases. This description tends to favor the aggregate form.

The wavelength-dependent ring particle phase function complicates the interpretation of spectrophotometric modeling, which gives information about the composition. Cuzzi and Estrada (1998) modeled the broadband ring particle albedo by making the assumption that the phase function was independent

of wavelength. Their conclusions that the meteoroid bombardment can explain the color ratios of Voyager images seems to be still qualitatively valid, but should be revalidated quantitatively by improving albedo modeling.

It is uncertain whether the reddening of rings continues at large α. CFD01 noted that the shape of the Voyager G/UV profile at 14° is qualitatively similar to the HST color ratio profile $C(0.555/0.336)$. Unfortunately, large uncertainties in the Voyager color calibration makes it impossible to use this data to draw conclusions about phase-dependent reddening between 6° and 14° (CFD01). Some asteroids and lunar samples exhibit a maximum in the α-dependence of the color ratio at α larger than 40° (Shkuratov *et al.* 1996). From measurements of a reddish silicate (Mars analog), Shkuratov *et al.* (1996) showed that the maximum shifts to the region of large α as the particle size decreases. It will not be possible to obtain observations at large α before the Cassini spacecraft reaches the Saturn system in 2004.

Observations at angles smaller than 0.3° could confirm or refute the trend that the decrease of the color ratio flattens or reverses close to opposition. We expect to detect this signature during HST observations in late 2002 or early 2003 when the phase angle reaches 0.15°.

The semi-rigorous photometric model of Shkuratov (1999) enables us to relate model parameters qualitatively to some physical properties of the regolith of ring particles. However, a number of refinements are needed before reliable quantitative interpretation can be made. Even though the laboratory data are still scarce, the Shkuratov theory shows a stronger grain size dependence of the CBOE amplitude than does the data (Fig. 2). As discussed in the paper, the OE of the C ring is best reproduced by the regime $d < \lambda < L$ while the grain sizes of the A and B rings are of the same order as $L(\gg \lambda)$. The grain size of the C ring can also be derived from the water ice absorption bands in the near-infrared, so that it will confirm or not the small derived size of the C ring grains. For a given size, higher albedo grains result in larger L/d than do lower albedo grains. Further work is needed to understand how lower albedo material can have larger L/d. Generally, a stronger connection needs to be made between the semi-empirical adjustable parameters of the theory (especially L) and actual grain properties (refractive index). We are addressing this in ongoing work.

ACKNOWLEDGMENTS

This work was performed while FP held a National Research Council (NASA Ames Research Center) research associateship. This work was supported in part by NASA Planetary Geology and Geophysics Program grants to JC (ARC 344-30-51-02) and RF (NAG5-4046), as well as by STSCI Grant GO-06806.01-95A. The work is based on observations with the NASA/ESA Hubble Space Telescope, obtained at the Space Telescope Science Institute, which is operated by the Association of Universities for Research in Astronomy, Inc., under NASA Contract NAS5-26555.

REFERENCES

Alix, J.-M. 1998. *Réflectivité et transmission des anneaux A et B de Saturne: Effets de la distribution de taille et nature physico-chimique des particules des anneaux.* Ph.D. dissertation, Université Paul Sabatier, Toulouse, France.

Belskaya, I. N., and V. G. Shevchenko 2000. Opposition effect of asteroids. *Icarus* **47**, 94–105.

Clark, R. N. 1980. Ganymede, Europa, Callisto, and Saturn's rings—Compositional analysis from reflectance spectroscopy. *Icarus* **44**, 388–409.

Clark, R. N., and T. B. McCord 1980. The rings of Saturn—New near-infrared reflectance measurements and a 0.326–4.08 micron summary. *Icarus* **43**, 161–168.

Cuzzi, J. N., and P. R. Estrada 1998. Compositional evolution of Saturn's rings due to meteoroid bombardment. *Icarus* **132**, 1–35.

Cuzzi, J. N., J. J. Lissauer, L. W. Esposito, J. B. Holberg, E. A. Marouf, G. L. Tyler, and A. Boischot 1984. Saturn's Rings: Properties and processes. In *Planetary Rings* (R. Greenberg and A. Brahic, Eds.), pp. 73–199. Univ. of Arizona Press, Tucson.

Cuzzi, J. N., R. G. French, and L. Dones 2001. HST multicolor (255–1042 nm) photometry of Saturn's main rings. I. Radial profiles, phase and opening angle variations, and regional spectra. *Icarus* **158**, 199–223.

Domingue, D. L., B. W. Hapke, G. W. Lockwood, and D. T. Thompson 1991. Europa's phase curve: Implications for surface structure. *Icarus* **90**, 30–42.

Domingue, D. L., G. W. Lockwood, and D. T. Thompson 1995. Surface textural properties of icy satellites: A comparison between Europa and Rhea. *Icarus* **115**, 228–249.

Dones, L., J. N. Cuzzi, and M. R. Showalter 1993. Voyager photometry of Saturn's A ring. *Icarus* **105**, 184–215.

Doyle, L. R., and E. Grün 1990. Radiative transfer modeling constraints on the size of the spoke particles in Saturn's rings. *Icarus* **85**, 168–190.

Doyle, L. R., L. Dones, and J. N. Cuzzi 1989. Radiative transfer modeling of Saturn's outer B ring. *Icarus* **80**, 104–135.

Drossart, P. 1993. Optics on a fractal surface and the photometry of the regoliths. *Planet. Space Sci.* **41**, 381–393.

Esposito, L. W., and K. Lumme 1977. The tilt effect for Saturn's rings. *Icarus* **31**, 157–167.

Franklin, F. A., and A. F. Cook 1965. Optical properties of Saturn's rings. II. Two-color phase curves of the 2 bright rings. *Astron J.* **70**, 704–720.

French, R. G., and P. D. Nicholson 2000. Saturn's rings. Particle sizes inferred from stellar occultation data. *Icarus* **145**, 502–523.

Hapke, B. 1981. Bidirectional reflectance spectroscopy. 1. Theory. *J. Geophys. Res.* **86**, 3039–3054.

Hapke, B. 1984. Bidirectional reflectance spectroscopy. 3. Correction for macroscopic roughness. *Icarus* **59**, 41–59.

Hapke, B. 1986. Bidirectional reflectance spectroscopy. 4. The extinction coefficient and the opposition effect. *Icarus* **67**, 264–280.

Hapke, B. 1990. Coherent backscatter and the radar characteristics of outer planet satellites. *Icarus* **88**, 407–417.

Hapke, B. 1999. Scattering and diffraction of ligth by particles in planetary regoliths. *J.Q.S.R.T.* **61**, 565–581.

Hapke, B., R. Nelson, and W. Smythe 1998. The opposition effect of the Moon: Coherent backscattering and shadow hiding. *Icarus* **133**, 89–97.

Helfenstein, P., J. Veverka, and P. C. Thomas 1988. Uranus satellites: Hapke parameters from Voyager disk-integrated photometry. *Icarus* **74**, 231–239.

Helfenstein, P., J. Veverka, and J. Hillier 1997. The lunar opposition effect: A test of alternative models. *Icarus* **128**, 2–14.

Helfenstein, P., and 21 colleagues 1998. Galileo observations of Europa's opposition effect. *Icarus* **135**, 41–63.

Hillier. J. K. 1997. Shadow-hiding opposition surge for a two-layer surface. *Icarus* **128**, 15–27.

Irvine, W. M. 1966. The shadowing effect in diffuse reflection. *J. Geophys. Res.* **71**, 2931–2937.

Liang, S., and M. I. Mishchenko 1997. Calculations of the soil hot-spot effect using the coherent backscattering theory. *Remote Sens. Environ.* **60**, 163–173.

Longaretti, P.-Y. **1989**, Saturn's main ring particle size distribution: An analytic approach. *Icarus* **81**, 51–73.

Lumme, K., and E. Bowell 1981a. Radiative transfer in the surfaces of atmosphereless bodies. I—Theory. *Astron. J.* **86**, 1694–1704.

Lumme, K., and E. Bowell 1981b. Radiative transfer in the surfaces of atmosphereless bodies. II. Interpretation *Astron. J.* **86**, 1705–1721.

Lumme, K., and W. M. Irvine 1976. Photometry of Saturn's rings *Astron. J.* **81**, 865–893.

Lumme, K., W. M. Irvine, and L. W. Esposito 1983. Theoretical interpretation of the ground-based photometry of Saturn's B ring. *Icarus* **53**, 174–184.

Marouf, E. A., G. L. Tyler, H. A. Zebker, R. A. Simpson, and V. R. Eshleman 1983. Particles size distributions in Saturn's rings from Voyager 1 radio occultation. *Icarus* **54**, 189–211.

Mishchenko, M. I. 1993. On the nature of the polarization opposition effect exhibited by Saturn's rings. *Astrophys. J.* **411**, 351–361.

Mishchenko, M. I., and Zh. M. Dlugach 1992. Can weak localization of photons explain the opposition effect of Saturn's rings? *Mon. Not. R. Astr. Soc.* **254**, 15P–18P.

Mishchenko, M. I., and Zh. M. Dlugach 1993. Coherent backscatter and the opposition effect for E-type asteroids. *Planet. Space Sci.* **41**, 173–181.

Muinonen, K. 1989. Electromagnetic scattering by two interacting dipoles. In *Proceedings 1989 URSI Electromagnetic Theory Symposium*, Stockholm, pp. 428–430.

Nelson, M. N., B. W. Hapke, W. D. Smythe, and L. J. Horn 1998. Phase curves of selected particulate materials: the contribution of coherent backscattering to the opposition surge. *Icarus* **131**, 223–230.

Nelson, M. N., B. W. Hapke, W. D. Smythe, and L. J. Spilker 2000. The opposition effect in simulated planetary regoliths. Reflectance and circular polarization ratio change at very small phase angle. *Icarus* **147**, 545–558.

Phroneen, J., K. Muinonen, S. Keranen, H. Karttunen, and J. Peltoniemi 2000. Backscattering of light by snow. In *Observing Land from Space: Science, Customers and Technology* (M. M. Verstraete, M. Menenti, and J. Peltoniemi, Eds.), pp. 219–228. Kluwer Academics, Dordrecht/Norwell, MA.

Pollack, J. B., A. Summers, and B. Baldwin 1973. Estimates of the size of the particles in the rings of Saturn and their cosmogonic implications. *Icarus* **20**, 263–278.

Richardson, D. C. 1994. Tree code simulations of planetary rings. *Mon. Not. R. Astr. Soc.* **269**, 493–511.

Rosen, P. A., G. L. Tyler, E. A. Marouf, and J. J. Lissauer 1991. Resonance structures in Saturn's rings probed by radio occultation. II Results and interpretation. *Icarus* **93**, 25–44.

Salo, H. 1987. Collisinal evolution of rotating particles. *Earth Moon Planets* **38**, 149–181.

Salo, H. 1992. Numerical simulations of dense collisional systems. II-Extended distribution of particle sizes. *Icarus* **96**, 85–106.

Shkuratov, Y. G., and P. Helfenstein 2001. The opposition effect and the quasi-fractal structure of regolith. *Icarus* **152**, 96–116.

Shkuratov, Y. G., L. Y. Melkumova, N. V. D. G. Opansenko, and D. G. Stankevich 1996. Phase dependence of the color indices of solid surfaces of celestial bodies. *Solar System Res.* **30**, 71–79.

Shkuratov, Y. G., A. A. Ovcharenko, D. G. Stankevich, and V. V. Korokhin 1997. A study of light backscattering from planetary-regolith-type surfaces at phase angles 0.2–3.5 degrees. *Solar System Res.* **31**, 56–63.

Shkuratov, Y. G., M. A. Kreslavsky, A. A. Ovcharenko, D. G. Stankevich, and E. S. Zubko 1999. Opposition effect from Clementine data and mechanisms of backscatter. *Icarus* **141**, 132–155.

Shu, F. H., L. Dones, J. J. Lissauer, C. Yuan, and J. N. Cuzzi 1985. Nonlinear spiral density waves: viscous damping. *Astrophys. J.* **299**, 542–573.

Weidenschilling, S. J., C. R. Chapman, D. R. Davis, and R. Greenberg 1984. Ring particles: Collisional interactions and physical nature. In *Planetary Rings* (R. Greenberg and A. Brahic, Eds.), pp. 367–416. Univ. of Arizona Press, Tucson.

Zebker H. A., E. A. Marouf, and G. L. Tyler 1985. Saturn's rings: Particles size distributions for thin layer model. *Icarus* **64**, 531–548.